NASA TECHNICAL NOTE

NASA TN D-3633

$\mathcal{C}.I$

AERODYNAMIC CHARACTERISTICS OF TENSION SHELL SHAPES AT MACH 3.0

by William D. Deveikis and James Wayne Sawyer

Langley Research Center

Langley Station, Hampton, Va.

NATIONAL AERONAUTICS AND SPACE ADMINISTRATION • WASHINGTON, D. C. • OCTOBER 1966
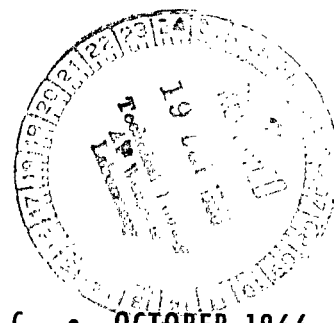
AERODYNAMIC CHARACTERISTICS OF TENSION

SHELL SHAPES AT MACH 3.0

By William D. Deveikis and James Wayne Sawyer

Langley Research Center
Langley Station, Hampton, Va.

NATIONAL AERONAUTICS AND SPACE ADMINISTRATION

AERODYNAMIC CHARACTERISTICS OF TENSION
SHELL SHAPES AT MACH 3.0

By William D. Deveikis and James Wayne Sawyer
Langley Research Center

SUMMARY

An investigation was conducted at a Mach number of 3.0 to determine aerodynamic characteristics of tension shell configurations for angles of attack from 0° to 12° and at free-stream Reynolds numbers, based on maximum body diameter, between approximately 1.0×10^6 and 3.0×10^6. The effects due to variations in the nose semivertex angle from 10° to 47°, ratios of nose radius to base radius from 0 to 0.4, and profile variations due to circumferential stress variations were observed. A group of catenary shapes was also tested. Short large-nose-angle bodies achieved axial-force coefficients to within 9 percent of the axial-force coefficient of a disk, were relatively insensitive to nose bluntness and flow separation effects, were statically stable, and approximated the force and moment variations with angle of attack of a 60° semivertex angle cone. Longer bodies with smaller nose angles developed axial-force coefficients up to 2 percent higher than the disk, but static stability was adversely affected by flow-separation effects.

INTRODUCTION

Because of their potential for attaining high drag and low structural mass, configurations termed tension shells are receiving attention for applications which require aerodynamic braking to decelerate from hypersonic to subsonic speeds. Although references 1, 2, and 3 are concerned with the use of tension shell shapes for unmanned planetary entry probes, the configurations are considered to be suitable for more general use as well. In view of the potential advantages offered by the concept, an experimental evaluation is in progress to determine the capabilities of tension shell shapes at various Mach numbers and Reynolds numbers. (See, for example, refs. 4 and 5.)

A typical tension shell (see fig. 1) is a thin axisymmetric shell or membrane which is intended to carry the aerodynamic loads primarily in tension and hence achieves high structural efficiency. The shape is characterized by negative Gaussian curvature, and is determined by using membrane theory in conjunction with an axisymmetric Newtonian pressure distribution to obtain specified ratios of circumferential stresses to meridional stresses. (See ref. 6.)

The purpose of the present investigation was to obtain aerodynamic-force measurements at a Mach number of 3 on a broad range of such shapes in which nose angle, nose radius, and body length were varied for two values of the stress ratio. Results were obtained at angles of attack up to 12° and at Reynolds numbers, based on maximum diameter, from approximately 1.0×10^6 to 3.0×10^6. The tests were conducted in the 9- by 6-inch model tunnel at the Langley Research Center.

SYMBOLS

The units used for the physical quantities defined in this paper are given in the U.S. Customary Units and in the International System of Units (SI) (ref. 7). Factors relating the two systems are given in the appendix.

A^2 shape parameter from reference 6 associated with Newtonian pressure

A_b base reference area, $\pi d^2/4$

C_A axial-force coefficient, $\dfrac{\text{Axial force}}{qA_b}$

C_D drag coefficient, $\dfrac{\text{Drag force}}{qA_b}$

C_m pitching-moment coefficient, $\dfrac{\text{Pitching moment}}{qA_b d}$

$C_{m_\alpha} = \dfrac{\partial C_m}{\partial \alpha}$ at $\alpha = 0^{\circ}$, per degree

C_N normal-force coefficient, $\dfrac{\text{Normal force}}{qA_b}$

$C_{N_\alpha} = \dfrac{\partial C_N}{\partial \alpha}$ at $\alpha = 0^{\circ}$, per degree

c catenary shape parameter from reference 6

d model-base diameter

L/D lift-drag ratio

l model length (fig. 2(b))

M free-stream Mach number

N_θ, N_φ	circumferential and meridional stresses, respectively
q	dynamic pressure
R	Reynolds number, the characteristic length of which is d
r	radial coordinate
r_b	model-base radius
r_n	spherical-nose radius
x	axial coordinate
α	angle of attack, degree
β	angle between body axis and tangent to surface at nose juncture, degree
β_o	nose semivertex angle for $r_n = 0$, degree

MODELS, APPARATUS, AND TESTS

Models

Three groups of tension shell shapes and three reference models were tested in this investigation. One group was a family of seven models with shapes derived by using membrane theory and an axisymmetric Newtonian pressure distribution to yield a membrane state of stress in which circumferential stresses were absent, that is, $\frac{N_\theta}{N_\varphi} = 0$. For these models, the membrane profile intersects the longitudinal axis at some angle β_o which is dependent upon the shape parameter A^2 and thus fixes the body length. (See fig. 2(a).) Hence, as β_o decreases, the body length increases. In this group of models, the angle β_o varied from 10° to 47° and corresponding ratios of length to base radius varied from 3.0 to 0.6. Each model was systematically blunted with four spherical nose radii for a range of ratios of nose radius to base radius from 0 to 0.4. Thus, the family of seven models yielded seven sets of five models each.

Another group consisted of two models with shapes which were derived with the requirement that circumferential tensile membrane stresses equal 15 percent of the meridional stresses, that is, $\frac{N_\theta}{N_\varphi} = 0.15$. The models were designed for comparison with

specific members from the family of seven models having nose angles β_0 of 31.8^O and 38.3^O (fig. 2(a)). These shapes were of interest because of their potential benefit in resisting membrane buckling which could occur at nonzero angles of attack where asymmetric loading would give rise to circumferential compressive membrane stresses. For these models, the membrane profiles were designed so that they fell slightly below their counterparts for $\frac{N_\theta}{N_\varphi} = 0$ and intersected them at an ordinate of $0.20r_b$, as illustrated in figure 2(b). Spherical caps were used to close the shapes at this ordinate on both pairs of the comparable models. Thus, the ratio of length to base radius, measured from the spherical nose juncture, was the same for comparable $\frac{N_\theta}{N_\varphi} = 0.15$ and $\frac{N_\theta}{N_\varphi} = 0$ models. The nose tangency angle β and the ratio of nose radius to base radius of the $\frac{N_\theta}{N_\varphi} = 0.15$ models were less than those of their $\frac{N_\theta}{N_\varphi} = 0$ counterparts.

In the third group were four catenary-shaped models which were also designed for comparison with members in the family of seven models, specifically those with nose angles β_0 of 21.5^O, 27.0^O, 31.8^O, and 47.0^O. These shapes were included because, as reported in reference 6, the catenary curve resembles the tension shell shape derived for $\frac{N_\theta}{N_\varphi} = 0.15$ and, when configured as a body of revolution, also possesses the structurally desirable properties of a tension shell. The models were designed by generating a catenary curve between the apex and base at radius r_b for lengths equal to the lengths of the comparable models for which $\frac{N_\theta}{N_\varphi} = 0$. The resulting catenary membrane profile fell below its counterpart for $\frac{N_\theta}{N_\varphi} = 0$ as shown in figure 2(c); and hence, the nose angle of the catenary-shaped models was smaller than that of the comparable $\frac{N_\theta}{N_\varphi} = 0$ models. Coordinates for the tension-shell-shaped models and catenary-shaped models are presented in tables I and II.

The reference models were a disk, a 45° semivertex angle cone, and a 60° semivertex angle cone. A photograph of typical models is shown in figure 3. The base diameter for all models was 1.25 inches (3.18 cm). All tension-shell-shaped models were constructed with square corners at the base, and the membrane profile of these models was tangent to the plane of the base at radius r_b. Hence, the airflow along the models was made to turn through an angle of 90°. The models were machined from commercially pure copper, and the surfaces were polished to a finish of approximately 10 microinches.

Test Facility

The models were tested in the 9- by 6-inch model tunnel at the Langley Research Center (ref. 8), a supersonic blowdown facility which exhausts to the atmosphere and

operates at a Mach number of 3.0. Calibration tests have shown that the maximum deviation in test-section Mach number is less than 1.0 percent.

The facility stagnation temperature range has been extended since the publication of reference 8 and presently operates over a range of stagnation temperatures from ambient to 3000° F $(1920^{\circ}$ K$)$ at stagnation pressures from 50 to 200 pounds per square inch $\left(345 \text{ to } 1380 \text{ kN/m}^2\right)$ absolute. These conditions yield a corresponding Reynolds number range of approximately 1.0×10^6 to 33×10^6 per foot. Stagnation temperatures above ambient are achieved by burning a mixture of air and propane in the settling chamber. This facility uses the air supply of the Langley 9- by 6-foot thermal structures tunnel which is sufficient to permit continuous operation of the model tunnel at ambient stagnation temperature.

Instrumentation

Aerodynamic forces and pitching moment were measured with the aid of a three-component strain-gage sting-balance assembly which was externally mounted relative to the model. An aerodynamic shroud shielded the sting and balance from the airstream. The model-sting-balance assembly is shown in the photograph of figure 4.

Model base pressure was measured at the upstream end of the shroud by means of an orifice tube located 90° from the vertical and attached along the outer surface of the shroud. One iron-constantan thermocouple was used to monitor model temperature at the base and it was located 180° from the base pressure orifice. Output from the strain-gage balance, pressure transducers, and thermocouples was recorded with the aid of the Langley central digital data recording facility.

Model shock waves and flow patterns were recorded by means of schlieren photography. The schlieren system is a single-pass, horizontal Z-type with a horizontal knife edge. A flashing light source and camera were synchronized to take photographs at the rate of 10 per second and at exposure times of a few microseconds.

The force and moment data presented herein were evaluated with the moment center located at a distance, upstream from the model base, of 50 percent of the base radius as shown in figure 1. Estimated maximum experimental errors are as follows:

$$C_A \quad \cdots \cdots \cdots \cdots \cdots \cdots \cdots \cdots \cdots \quad \pm 0.020$$

$$C_D \quad \cdots \cdots \cdots \cdots \cdots \cdots \cdots \cdots \cdots \quad \pm 0.020$$

$$C_D \quad \text{(figs. 11 and 12)} \quad \cdots \cdots \cdots \quad \pm 0.040$$

$$C_m \quad \cdots \cdots \cdots \cdots \cdots \cdots \cdots \cdots \quad \pm 0.010$$

$$C_N \quad \cdots \cdots \cdots \cdots \cdots \cdots \cdots \cdots \quad \pm 0.010$$

$$M \quad \cdots \cdots \cdots \cdots \cdots \cdots \cdots \cdots \quad \pm 0.03$$

All tests were conducted at ambient stagnation temperature and at discrete stagnation pressures up to 170 pounds per square inch (1170 kN/m^2) absolute. Corresponding Reynolds numbers, based on maximum diameter, ranged from approximately 1.0×10^6 to 3.0×10^6. All models, except the disk reference model, were tested at angles of attack from 0° to 12° in 3° increments. The ratio of model temperature to stagnation temperature was approximately 0.97.

The test procedure was to start the tunnel with the model set at an angle of attack of 0° and to maintain a stagnation pressure of 60 pounds per square inch (414 kN/m^2) absolute until the model temperature reached equilibrium. Data were then recorded at stagnation pressures of 60, 100, 130, and 170 pounds per square inch (414, 690, 896, and 1170 kN/m^2) absolute. The stagnation pressure was returned to the low level prior to each change in angle of attack. Each stagnation-pressure level was maintained for approximately 5 seconds to ensure an equilibrium-model base-pressure response.

RESULTS AND DISCUSSION

$$\text{Models for} \quad \frac{N_\theta}{N_\varphi} = 0$$

The results presented herein for the family of seven shapes derived for $\dfrac{N_\theta}{N_\varphi} = 0$ were obtained from duplicate sets of models. One set was used to obtain drag data only at $\alpha = 0^\circ$ and was the same set of models used in the tests of reference 5. A duplicate set was constructed and tested to obtain force and moment data at $\alpha > 0^\circ$; for these tests a strain-gage balance different from that used in the tests of the first set of models was used. All experimental drag and axial-force data presented are corrected to a free-stream static-pressure condition at the model base. Actual measured C_D and C_A values were approximately 0.11 higher than those shown.

Effects of nose angle and nose radius on flow pattern at $\alpha = 0^\circ$.- Representative flow patterns which reflect the effects of nose angle (and hence, body length) and nose radius at zero angle of attack are shown in the schlieren photographs of figures 5 to 9. The photographs were taken when the Reynolds number was approximately 3.0×10^6. In each figure, the models are shown in ascending order of the nose angle β_0 for a constant ratio of nose radius to base radius r_n/r_b. Schlieren photographs of the blunted models for $\beta_0 = 10.1^\circ$ and 15.8° were not available. The photographs show that boundary-layer-flow separation was encountered on many of the models. The extent of the flow separation was dependent on nose angle and nose radius and, as will be shown subsequently, had a pronounced effect on the aerodynamic characteristics.

Typical effects of nose-angle variations on flow patterns can be ascertained from the flow patterns of the pointed models $(r_n/r_b = 0)$ shown in figure 5. The photographs show that decreasing the nose angle from $\beta_0 = 47^\circ$ generates flow patterns ranging from those in which the flow around the model is entirely subsonic, as in figure 5(g) where a detached bow wave is shown, to those in which both subsonic and supersonic flow are present as characterized by the double shock waves seen in figures 5(c) to 5(f) for $\beta_0 = 21.5^\circ$ to 38.3°. Both types of flow patterns suggest a high pressure recovery on the model near the base. For the shapes with the double shock wave, the standoff distance of the standing wave ahead of the base decreases from approximately 36 to 26 percent of the base diameter as the nose angle β_0 decreases from 38.5° to 21.5°. When the nose angle is decreased from $\beta_0 = 21.5^\circ$, boundary-layer-flow separation is induced upstream of the standing wave as shown in figures 5(a) and 5(b). In this case, the model shape at the base is essentially shielded by the separated boundary layer and is, therefore, rendered ineffective in developing a high pressure recovery.

Similar changes in flow pattern with nose angle occur when the nose is blunted. (See figs. 6 to 9.) However, as the nose radius increases, boundary-layer-flow separation is induced on progressively shorter models $\left(\text{larger } \beta_0\right)$ for β_0 up to 31.8°. Therefore, inasmuch as other photographs often showed a downstream movement of the separation point as Reynolds number was increased, it appears that a higher Reynolds number is required to maintain an attached boundary layer as the nose radius is increased.

The effects on flow behavior due to nose angle and nose radius are summarized in figure 10 where the range of β_0 over which flow separation occurred for each r_n/r_b is shown. Approximately 50 percent of the models from the family of seven shapes encountered flow separation at $\alpha = 0^\circ$. The models for $\beta_0 = 38.5^\circ$ and 47.0° did not encounter flow separation at any r_n/r_b, and of these models, the flow pattern for $\beta_0 = 47.0^\circ$ appeared to be unaffected by a variation in nose radius.

Drag at $\alpha = 0^\circ$.- The highest drag coefficients at $\alpha = 0^\circ$ were obtained from the models on the attached-flow side of the boundary in figure 10. This effect is shown in figure 11(a), where C_D at a Reynolds number of approximately 3.0×10^6 is plotted against β, the angle between the body axis and the tangent to the surface at the nose juncture for each r_n/r_b. The angle β increases with r_n/r_b for each set of models of a given β_0. The C_D values of the models for $\beta > 38.3^\circ$ are within 9 percent of the disk, and like their flow patterns, are relatively insensitive to nose radius variations. As the nose angle is decreased, C_D increases until flow separation is encountered and then drops rapidly. The actual measured (uncorrected) value for $\beta = 21.7^\circ$ at $r_n/r_b = 0$ was 3 percent higher than the stagnation pressure coefficient behind a normal shock.

The trend toward higher experimental values of C_D with decreasing nose angle is at variance with the theoretical trends shown and is due to the increasing amount of flow which passes through the oblique shock wave ahead of the standing wave. Hence, a higher pressure recovery is effected on the rear portion of the model as the nose angle decreases. As is evident from the photographs of figures 5 to 9, the discrepancy between Newtonian theory and experiment arises from a departure from a basic theoretical assumption which states that the shock wave is wrapped closely around the body so that the flow through the shock wave at any point is turned through an angle equal to the slope of the body. Moreover, the local surface pressures behind the standing wave on the models with the double shock wave would be expected to deviate from Newtonian values because of the shock waves seen reflecting between the surface and the slip plane which emanates from the intersection of the oblique and standing waves.

Drag coefficients obtained with the same set of models tested at $M = 7$ when $R = 0.08 \times 10^6$ and reported in reference 5 are shown in figure 11(b) for comparison with the present data. The chief difference in drag performance at the two Mach numbers is that the abrupt drop in C_D due to the onset of flow separation occurs at smaller nose angles at $M = 3$ than at $M = 7$ for a given r_n/r_b. Consequently, most of the C_D values are higher at $M = 3$. Inasmuch as the onset of flow separation at $M = 3$ appeared to be dependent on Reynolds number, it is possible that the higher C_D values at $M = 3$ reflect the Reynolds number difference in the tests. At the largest nose angles, however, the C_D values at $M = 7$ are up to 7 percent higher than those at $M = 3$.

Reynolds number effects on drag.- The effects on C_D due to changes in Reynolds number were most consistent for the models with attached flow and also for those cases in which the flow separation point was essentially stationary. In such instances, an increase in Reynolds number resulted in only a slight decrease in C_D. In other instances, where the separation point moved downstream with increase in Reynolds number, C_D showed a slight increase. Large and erratic effects on C_D due to changes in the Reynolds number occurred on models when the separation point oscillated along the model length. Typical examples reflecting these effects are shown in figure 12, where C_D is plotted against Reynolds number for models with $\beta_0 = 21.5^\circ$ and all r_n/r_b at $\alpha = 0^\circ$.

Effects of nose angle and nose radius on flow pattern at small angles of attack.- Although the models with an attached boundary layer developed high drag coefficients at $\alpha = 0^\circ$, most of them encountered leeward flow separation at other angles of attack. For some models, leeward flow separation occurred at angles of attack as low as 3° as shown, for example, in figure 13. A history, compiled from photographic data, of the

flow-separation experience of the models for β_o between 21.5° and 47.0° and all r_n/r_b over the angle of attack and Reynolds number ranges of the tests is presented in table III. The table shows that leeward flow separation was encountered at $\alpha > 0°$ on all pointed models for $\beta_o \leqq 31.8°$ and on all blunted models for $\beta_o \leqq 38.3°$. The models for $\beta_o = 47.0°$ did not encounter flow separation at any α, r_n/r_b, or Reynolds number. The trend of α for leeward flow separation is to decrease as β_o decreases and as r_n/r_b increases and for some models, to increase with Reynolds number.

Aerodynamic characteristics at small angles of attack.- The aerodynamic characteristics of the models for $\beta_o > 21.5°$ at all r_n/r_b and of the two cone reference models are presented in figure 14 over the angle-of-attack range of the tests for a Reynolds number of approximately 3.0×10^6. Data from the models for $\beta_o < 21.5°$ were omitted because of their poor drag performance at $\alpha = 0°$.

The shortest models ($\beta_o = 47.0°$ and $38.3°$, figs. 14(a) and 14(b)) maintained a high axial-force coefficient with angle of attack and showed linear variations of pitching-moment coefficient, normal-force coefficient, and lift-drag ratio. Except for a larger effect on C_D of the models for $\beta_o = 38.3°$, the aerodynamic characteristics of these shorter models were virtually unaffected by variations in nose radius, even though leeward flow separation was encountered by the models for $\beta_o = 38.3°$ at $r_n/r_b > 0$. (See table III.)

In general, similar variations in axial-force and pitching-moment coefficients with angle of attack were also obtained with the longer models ($\beta_o < 38.3°$) when the boundary layer remained attached. However, the occurrence of leeward flow separation often resulted in a sudden decrease in the axial-force coefficient and pitching-moment coefficient and a corresponding increase in the normal-force coefficient and lift-drag ratio as shown in figures 14(c) to 14(e). This abrupt shift in coefficient direction reflected a rapid upstream movement of the separation point to the tip. The actual angle of attack for leeward separation at the tip was unknown and is, therefore, shown as a dashed line in the faired curves. After the sudden onset of leeward flow separation, the trend of the pitching-moment coefficient with angle of attack was toward positive values and hence negative static stability. A more gradual change in coefficient direction was recorded when the leeward separation point moved gradually upstream as shown, for example, in figure 14(e) for $\beta_o = 21.5°$ and $r_n/r_b = 0$ up to $\alpha = 6°$.

Limitations on the measurement accuracy and the small values of normal-force and pitching-moment coefficients prevented accurate determination of model center-of-pressure locations. The best estimates based on values of the parameters C_{m_α} and C_{N_α} (slopes of the pitching-moment- and normal-force-coefficient curves, respectively, evaluated at $\alpha = 0°$) indicated that the center of pressure was located behind the model

base in those cases for which C_{m_α} was negative and generally ahead of the model nose when C_{m_α} was positive. Because of the extensive flow separation experienced at $\alpha > 0^O$, estimation of C_{m_α} was restricted to the values shown in table IV and was obtained only for those shapes which showed attached flow at $\alpha = 0^O$ and 3°. For the shortest model ($\beta_0 = 47.0^O$), the static stability approximated that of the 60° cone.

$$\text{Models for } \frac{N_\theta}{N_\varphi} = 0.15$$

Schlieren photographs of the two models designed for $\frac{N_\theta}{N_\varphi} = 0.15$ and the comparable $\frac{N_\theta}{N_\varphi} = 0$ models are shown in figures 15 and 16. The shortest $\frac{N_\theta}{N_\varphi} = 0.15$ model showed a steep, detached bow wave similar to that of its $\frac{N_\theta}{N_\varphi} = 0$ counterpart. Although its nose angle and ratio of nose radius to base radius placed the $\frac{N_\theta}{N_\varphi} = 0.15$ model very close to the faired flow separation boundary of figure 10, neither of the shorter models encountered boundary-layer separation at $\alpha = 0^O$. However, both of the shorter models did encounter leeward separation at $\alpha > 0^O$, but the angle of attack for leeward separation was smaller for the $\frac{N_\theta}{N_\varphi} = 0.15$ model. Inasmuch as the flow patterns of the shorter pair of comparable models were not very different at $\alpha > 0^O$, their aerodynamic characteristics were nearly identical as shown by the data of figure 17(a).

The schlieren photographs of the longer pair of models (fig. 16) showed that the boundary layer separated from both models at $\alpha = 0^O$. In this case, the nose angle and the ratio of nose radius to base radius of the $\frac{N_\theta}{N_\varphi} = 0.15$ model were well within the separated-flow region of figure 10; whereas, those of the $\frac{N_\theta}{N_\varphi} = 0$ model lay very close to the faired flow-separation boundary. For the $\frac{N_\theta}{N_\varphi} = 0.15$ model, the flow was very unsteady and was characterized by a flow pattern wherein the shock wave alternately expanded and collapsed as in figures 16(b) and 16(c). At $\alpha > 0^O$, the angle of attack for windward boundary-layer attachment was greater for the $\frac{N_\theta}{N_\varphi} = 0.15$ model and the axial-force performance of the $\frac{N_\theta}{N_\varphi} = 0.15$ model was degraded with respect to its $\frac{N_\theta}{N_\varphi} = 0$ counterpart (fig. 17(b)). Thus, a small reduction in membrane profile ordinates can lead

to detrimental effects, chief among which is the inducement of flow separation at smaller angles of attack which can adversely alter aerodynamic characteristics.

Catenary-Shaped Models

Whereas flow separation at $\alpha = 0^\circ$ was induced on the $\frac{N_\theta}{N_\varphi} = 0$ models when the nose angle and body length, respectively, decreased and increased simultaneously, the results from the catenary model tests showed that flow separation can also be induced by decreasing the nose angle while maintaining a fixed body length. Thus, the substantially smaller nose angle of the longest catenary-shaped model ($\beta_0 = 13.9^\circ$) with respect to its $\frac{N_\theta}{N_\varphi} = 0$ counterpart ($\beta_0 = 21.5^\circ$) was sufficient to place it within the separated flow region of figure 10. Consequently, the drag coefficient of the longest catenary-shaped model at $\alpha = 0^\circ$ was much less than its $\frac{N_\theta}{N_\varphi} = 0$ counterpart of equal length. Nevertheless, some degree of correlation between the drag coefficients of both model groups is achieved when C_D is plotted against β_0 as in figure 18. In this figure, the drag coefficients from both sets of pointed $\frac{N_\theta}{N_\varphi} = 0$ models are shown.

The aerodynamic characteristics of the catenary-shaped models showed the same trends with angle of attack and the same dependence on the character of the boundary layer as the $\frac{N_\theta}{N_\varphi} = 0$ models. (See fig. 19.) However, greater changes in coefficient values of the catenary-shaped models occurred at the onset of leeward separation, and the angle of attack for leeward separation was smaller for the catenary-shaped models with respect to their $\frac{N_\theta}{N_\varphi} = 0$ counterparts. Only one of the catenary-shaped models, the shortest ($\beta_0 = 37.2^\circ$), showed static stability based on an estimate of the center-of-pressure location.

CONCLUSIONS

An investigation was conducted at a Mach number of 3.0 to determine the aerodynamic characteristics of a number of axisymmetric configurations called tension shells which were derived from a structural concept considered potentially useful in applications requiring aerodynamic braking from hypersonic speeds. Model shapes varied in length such that the ratio of length to base radius ranged from 0.6 to 3.0 as the nose semivertex angle varied from 47° to 10°. The ratio of nose radius to base radius was varied from 0 to 0.4. The tests were conducted at angles of attack up to 12°, at Reynolds

numbers, based on maximum body diameter, from approximately 1.0×10^6 to 3.0×10^6, and at a ratio of model temperature to stagnation temperature of approximately 0.97.

The results indicated the following:

1. The onset of boundary-layer-flow separation was dependent on the nose angle, body length, nose radius, and Reynolds number. Flow separation was induced on progressively shorter models as the nose radius was increased.

2. Schlieren photographs indicated that the assumption of Newtonian flow used in the derivation of the model shapes is not valid.

3. High drag coefficients were obtained at an angle of attack of 0° when the boundary layer was attached. Values ranged from within 9 percent of that of a reference disk model (adjusted to free-stream pressure at the base) to an actual measured value 3 percent higher than the stagnation pressure coefficient behind a normal shock.

4. The force and moment coefficient variations with angle of attack were smooth and nearly linear when the boundary layer was attached, whereas flow separation from the leeward side caused a sudden decrease in axial-force and pitching-moment coefficients.

5. Of the models without flow separation, the force and moment data indicated static stability only for the shortest models; the stability of these models approximated that of a 60° semivertex angle cone.

Langley Research Center,
National Aeronautics and Space Administration,
Langley Station, Hampton, Va., May 4, 1966.

APPENDIX

CONVERSION OF U.S. CUSTOMARY UNITS TO SI UNITS

The International System of Units (SI) was adopted by the Eleventh General Conference on Weights and Measures held in Paris, October 1960, in Resolution No. 12 (ref. 7). Conversion factors required for units used herein are given in the following table:

Physical quantity	U.S. Customary Unit	Conversion factor (*)	SI Unit
Length	in.	0.0254	meters (m)
Pressure	lb/sq in.	6.895×10^3	newtons/meter^2 (N/m^2)
Temperature	(F^O + 460)	5/9	degrees Kelvin (^{O}K)

*Multiply value given in U.S. Customary Unit by conversion factor to obtain equivalent value in SI Unit.

Prefixes to indicate multiples of units are as follows:

Prefixes	Multiple
centi (c)	10^{-2}
hecto (h)	10^2
kilo (k)	10^3
mega (M)	10^6
giga (G)	10^9

REFERENCES

1. Roberts, Leonard: Entry Into Planetary Atmospheres. Astronaut. Aeron., vol. 2, no. 10, Oct. 1964, pp. 22-29.

2. Anderson, Roger A.: Structures Technology — 1964. Astronaut. Aeron., vol. 2, no. 12, Dec. 1964, pp. 14-20.

3. Guy, L. D.: Tension Shell Structures for Low Density Entry Vehicles. Presented at AIAA Second Annual Meeting and Technical Display (San Francisco, Calif.), July 1965.

4. Bernot, Peter T.: Longitudinal Stability Characteristics of Several Proposed Planetary Entry Vehicles at Mach 6.73. NASA TN D-2785, 1965.

5. Robinson, James C.; and Jordan, Alfred W.: Exploratory Experimental Aerodynamic Investigation of Tension Shell Shapes at Mach 7. NASA TN D-2994, 1965.

6. Anderson, Melvin S.; Robinson, James C.; Bush, Harold G.; and Fralich, Robert W.: A Tension Shell Structure for Application to Entry Vehicles. NASA TN D-2675, 1965.

7. Mechtly, E. A.: The International System of Units — Physical Constants and Conversion Factors. NASA SP-7012, 1964.

8. Schaefer, William T., Jr.: Characteristics of Major Active Wind Tunnels at the Langley Research Center. NASA TM X-1130, 1965.

TABLE I.- COORDINATES OF TENSION SHELL SHAPES

r/r_b	x/r_b for –								
	$N_\theta/N_\varphi = 0$							$N_\theta/N_\varphi = 0.15$	
	$\beta_0 = 10.1^\circ$ $(A^2 = 2.427)$	$\beta_0 = 15.8^\circ$ $(A^2 = 1.973)$	$\beta_0 = 21.5^\circ$ $(A^2 = 1.663)$	$\beta_0 = 27.0^\circ$ $(A^2 = 1.423)$	$\beta_0 = 31.8^\circ$ $(A^2 = 1.257)$	$\beta_0 = 38.3^\circ$ $(A^2 = 1.058)$	$\beta_0 = 47.0^\circ$ $(A^2 = 0.835)$	$\beta = 23.5^\circ$ $(A^2 = 1.050)$	$\beta = 32.1^\circ$ $(A^2 = 0.900)$
0	3.000	2.000	1.500	1.192	1.000	0.800	0.600	(*)	(**)
.05	2.720	1.824	1.373	1.094	.919	.737	.554	(*)	(**)
.10	2.443	1.650	1.247	.998	.839	.674	.507	(*)	(**)
.15	2.172	1.479	1.124	.901	.760	.612	.462	(*)	(**)
.20	1.912	1.314	1.004	.808	.683	.551	.417	0.696	0.555
.25	1.664	1.155	.888	.718	.608	.492	.373	.593	.481
.30	1.431	1.004	.776	.630	.536	.435	.331	.507	.416
.35	1.215	.862	.672	.549	.467	.380	.290	.432	.357
.40	1.017	.731	.513	.469	.402	.328	.251	.365	.303
.45	.837	.610	.481	.397	.341	.279	.216	.305	.255
.50	.673	.500	.398	.330	.284	.234	.180	.251	.211
.55	.537	.400	.323	.269	.232	.192	.148	.203	.171
.60	.415	.314	.255	.214	.185	.153	.119	.160	.136
.65	.310	.239	.195	.165	.143	.119	.092	.123	.104
.70	.223	.174	.143	.122	.106	.088	.069	.091	.077
.75	.153	.120	.100	.085	.074	.062	.049	.063	.054
.80	.096	.076	.064	.054	.048	.040	.032	.041	.035
.85	.053	.043	.036	.030	.027	.023	.018	.023	.020
.90	.023	.019	.016	.014	.013	.011	.008	.010	.009
.95	.005	.005	.004	.004	.003	.003	.002	.003	.002
1.00	.000	.000	.000	.000	.000	.000	.000	.000	.000

*$\dfrac{r_n}{r_b} = 0.217.$

**$\dfrac{r_n}{r_b} = 0.236.$

TABLE II.- COORDINATES OF CATENARY SHAPES

r/r_b	x/r_b for —			
	$\beta_O = 13.9^O$ (c = 0.297)	$\beta_O = 18.4^O$ (c = 0.343)	$\beta_O = 24.1^O$ (c = 0.387)	$\beta_O = 37.2^O$ (c = 0.574)
0	1.500	1.192	1.000	0.600
.05	1.309	1.049	.884	.537
.10	1.138	.919	.778	.477
.15	.984	.805	.682	.423
.20	.847	.694	.593	.371
.25	.724	.597	.513	.324
.30	.615	.510	.440	.280
.35	.518	.432	.374	.240
.40	.431	.362	.314	.203
.45	.355	.299	.261	.170
.50	.288	.244	.211	.140
.55	.229	.195	.171	.113
.60	.178	.152	.134	.088
.65	.135	.115	.102	.068
.70	.098	.084	.074	.049
.75	.067	.058	.051	.034
.80	.047	.037	.033	.022
.85	.026	.021	.018	.012
.90	.011	.009	.008	.005
.95	.003	.002	.002	.001
1.00	.000	.000	.000	.000

TABLE III.- HISTORY OF BOUNDARY-LAYER SEPARATION EVENTS

$\dfrac{r_n}{r_b}$	R	Surface	Occurrence of separated flow for -																							
			$\beta_o = 21.5°$					$\beta_o = 27.0°$					$\beta_o = 31.8°$					$\beta_o = 38.3°$					$\beta_o = 47.0°$				
			Angle of attack, deg																								
			0	3	6	9	12	0	3	6	9	12	0	3	6	9	12	0	3	6	9	12	0	3	6	9	12
0	1.0×10^6	Leeward																										
		Windward																										
	1.7×10^6	Leeward																										
		Windward																										
	2.3×10^6	Leeward																										
		Windward																										
	3.0×10^6	Leeward																										
		Windward																										
0.05	1.0×10^6	Leeward																										
		Windward																										
	1.7×10^6	Leeward																										
		Windward																										
	2.3×10^6	Leeward																										
		Windward																										
	3.0×10^6	Leeward																										
		Windward																										
0.10	1.0×10^6	Leeward																										
		Windward																										
	1.7×10^6	Leeward																										
		Windward																										
	2.3×10^6	Leeward																										
		Windward																										
	3.0×10^6	Leeward																										
		Windward																										
0.20	1.0×10^6	Leeward																										
		Windward																										
	1.7×10^6	Leeward																										
		Windward																										
	2.3×10^6	Leeward																										
		Windward																										
	3.0×10^6	Leeward																										
		Windward																										
0.40	1.0×10^6	Leeward																										
		Windward																										
	1.7×10^6	Leeward																										
		Windward																										
	2.3×10^6	Leeward																										
		Windward																										
	3.0×10^6	Leeward																										
		Windward																										

▦ Separated flow

TABLE IV.- STABILITY PARAMETER OF $\dfrac{N_\theta}{N_\varphi} = 0$ TENSION SHELL SHAPES

$$\left[R \approx 3.0 \times 10^6\right]$$

β_o, deg	C_{m_α} for r_n/r_b of —				
	0	0.05	0.10	0.20	0.40
47.0	−0.0015	−0.0018	−0.0023	−0.0020	−0.0023
38.3	−.0007	−.0006	-----	-----	−.0006
31.8	.0020	.0026	-----	-----	−.0001
27.0	.0027	-----	-----	-----	-----
60° cone	−.0030	-----	-----	-----	-----
45° cone	−.0062	-----	-----	-----	-----
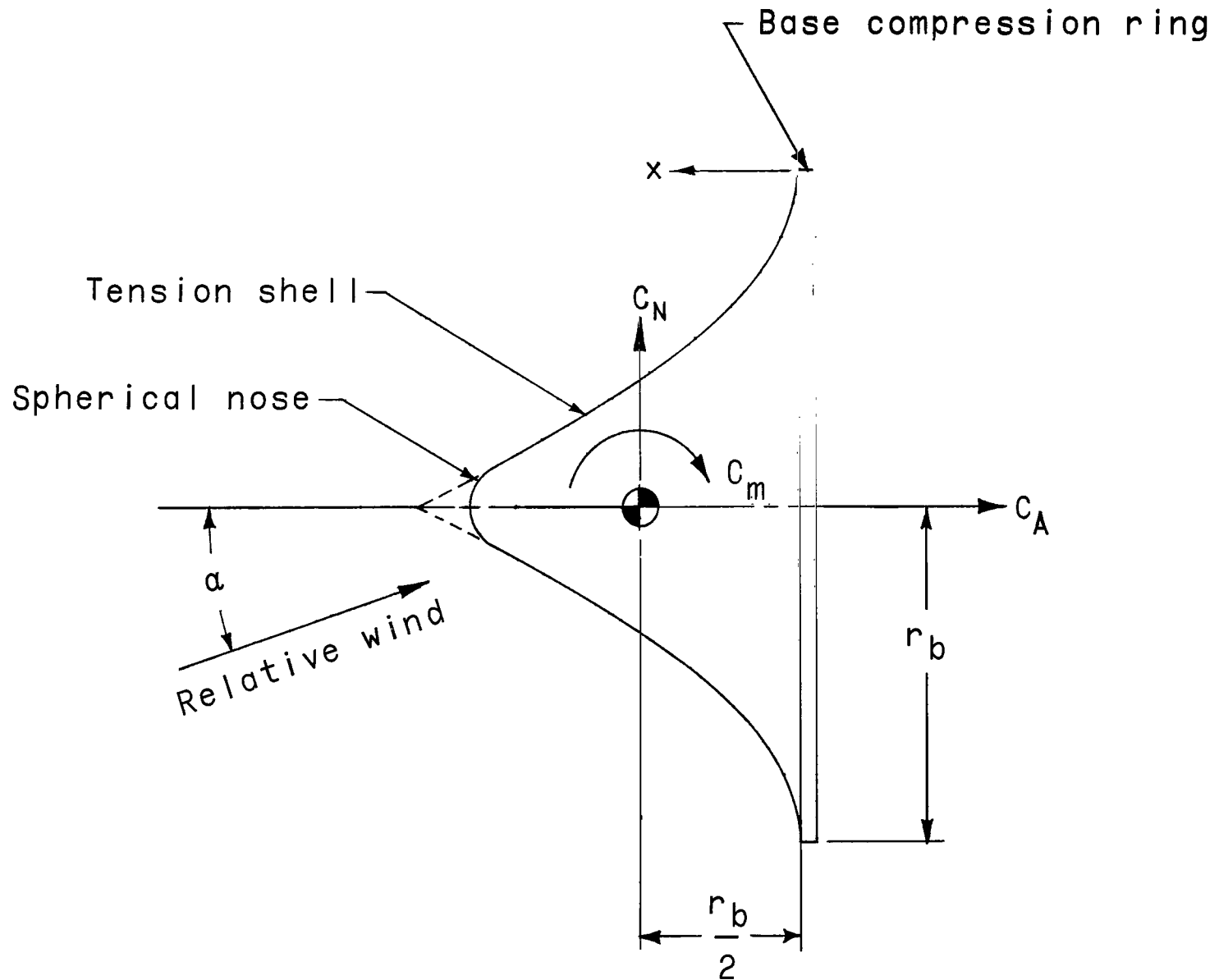
Figure 1.- Body axis system. Arrows indicate positive directions.

(a) Family of $\dfrac{N_\theta}{N_\varphi} = 0$ models.

N_θ/N_φ	β, deg	l/r_b	r_n/r_b
0	39.8	0.555	0.260
0	32.9	.696	.238
.15	32.1	.555	.236
.15	23.5	.696	.218

Catenary	$N_\theta/N_\varphi = 0$
β_o, deg	
14.0	21.5
18.4	27.0
24.1	31.8
37.3	47.0
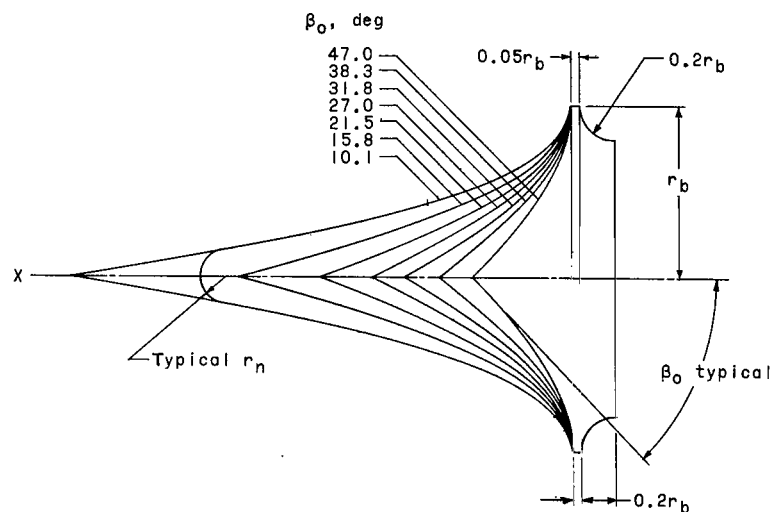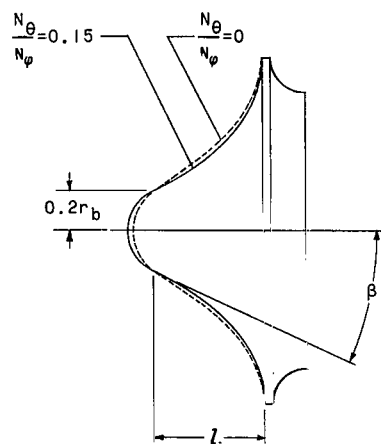
(b) Comparison of typical $\dfrac{N_\theta}{N_\varphi} = 0$ and $\dfrac{N_\theta}{N_\varphi} = 0.15$ models.

(c) Comparison of typical catenary and $\dfrac{N_\theta}{N_\varphi} = 0$ models.

Figure 2.- Model details. Maximum body radius $r_b = 0.625$ in. (1.59 cm).
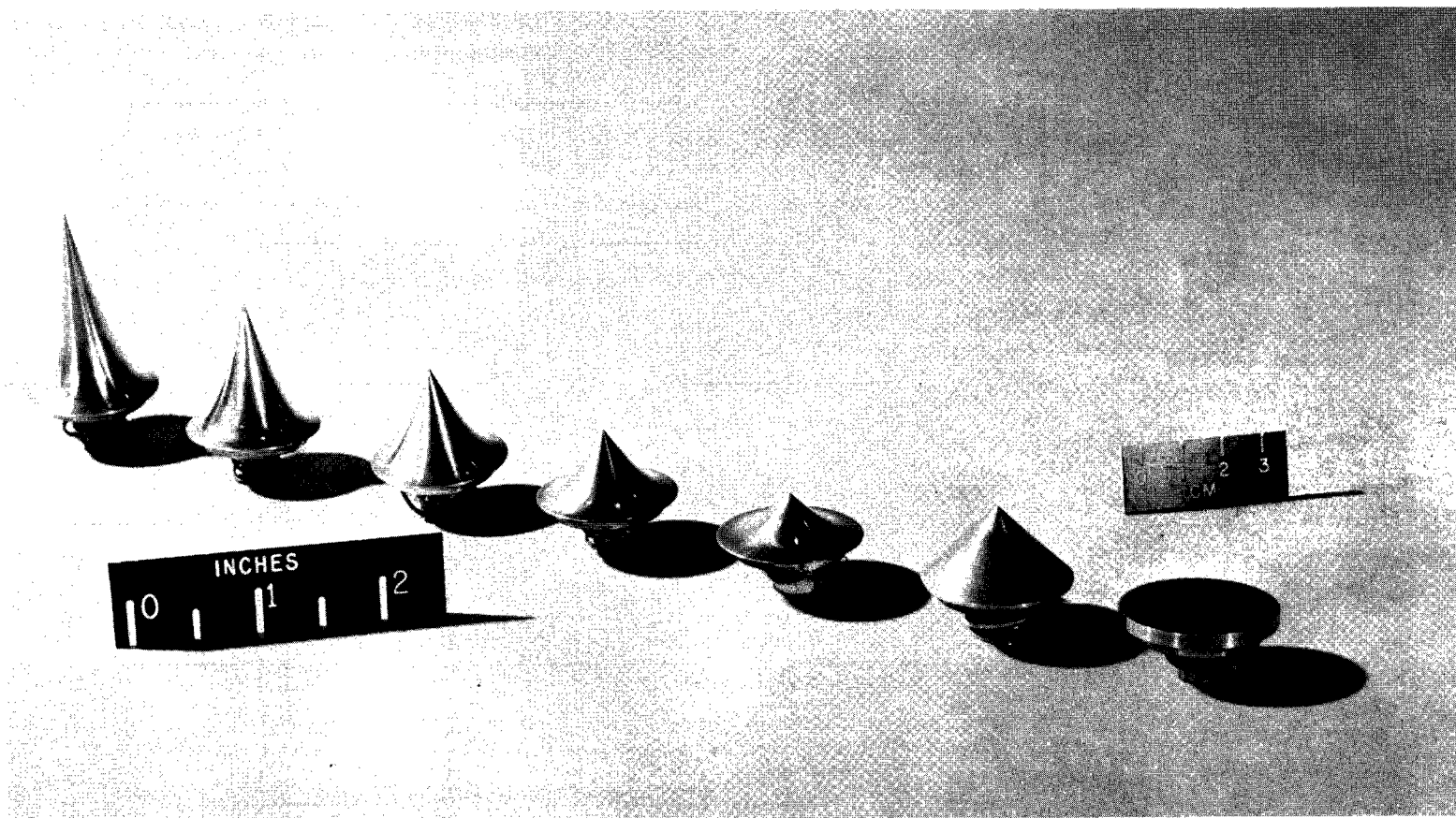
Figure 3.- Photograph of typical group of tension shell models and reference cone and disk models.

L-64-5499

21
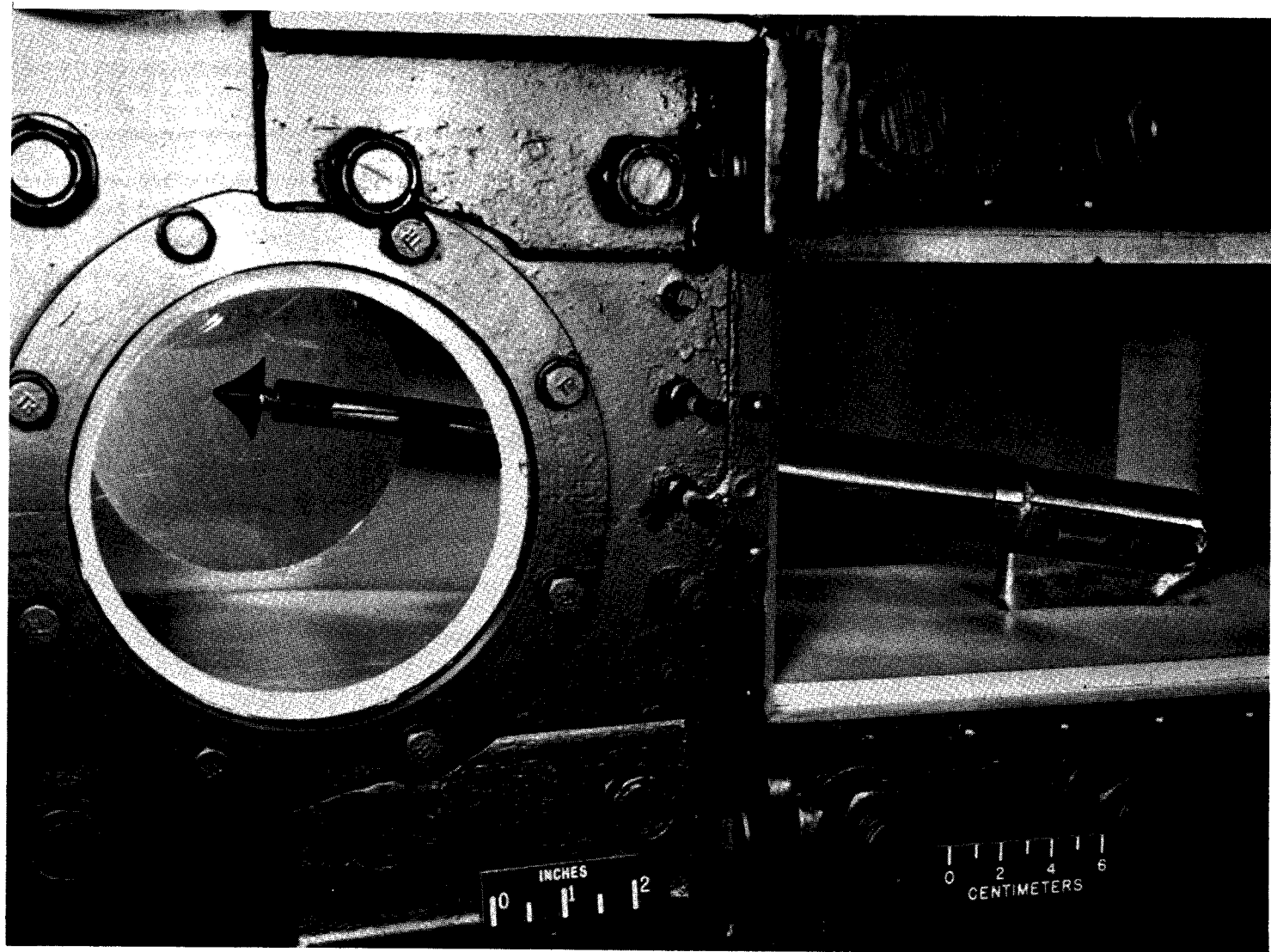
Figure 4.- Photograph of model-sting-balance assembly mounted in test section of 9- by 6-inch model tunnel.

L-65-7524

(a) $\beta_0 = 10.1^0$.

(b) $\beta_0 = 15.8^0$.

Figure 5.- Schlieren photographs of $\dfrac{N_\theta}{N_\varphi} = 0$ tension shell shapes. $\dfrac{r_n}{r_b} = 0$; $\alpha = 0^0$; $R \approx 3.0 \times 10^6$.
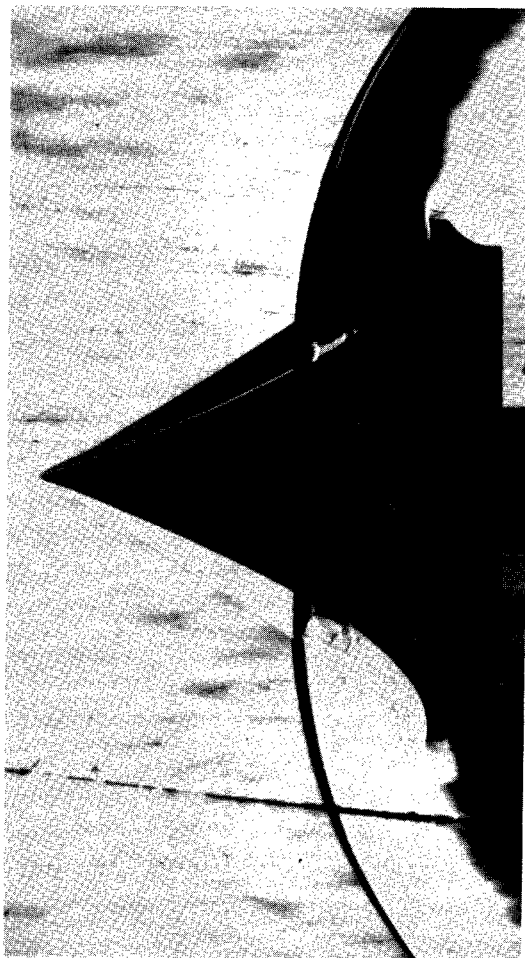
L-66-4401

(c) $\beta_0 = 21.5^0$.

(d) $\beta_0 = 27.0^0$.

(e) $\beta_0 = 31.8^0$.

Figure 5.- Continued.

L-66-4402
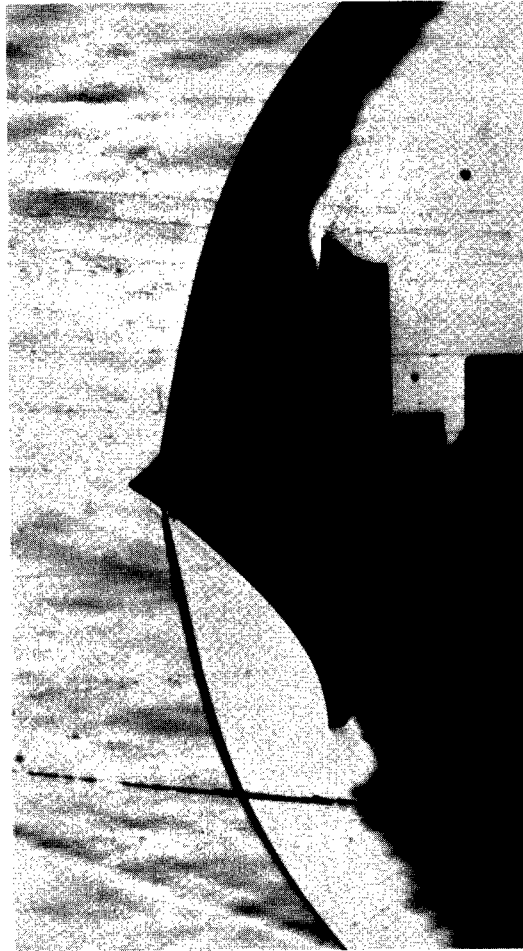
(f) $\beta_0 = 38.3^0$.

(g) $\beta_0 = 47.0^0$.

Figure 5.- Concluded.

26

(a) $\beta_0 = 21.5^0$.   (b) $\beta_0 = 27.0^0$.   (c) $\beta_0 = 31.8^0$.

Figure 6.- Schlieren photographs of $\frac{N_\theta}{N_\varphi} = 0$ tension shell shapes. $\frac{r_n}{r_b} = 0.05$; $\alpha = 0^0$, $R \approx 3.0 \times 10^6$.   L-66-4404
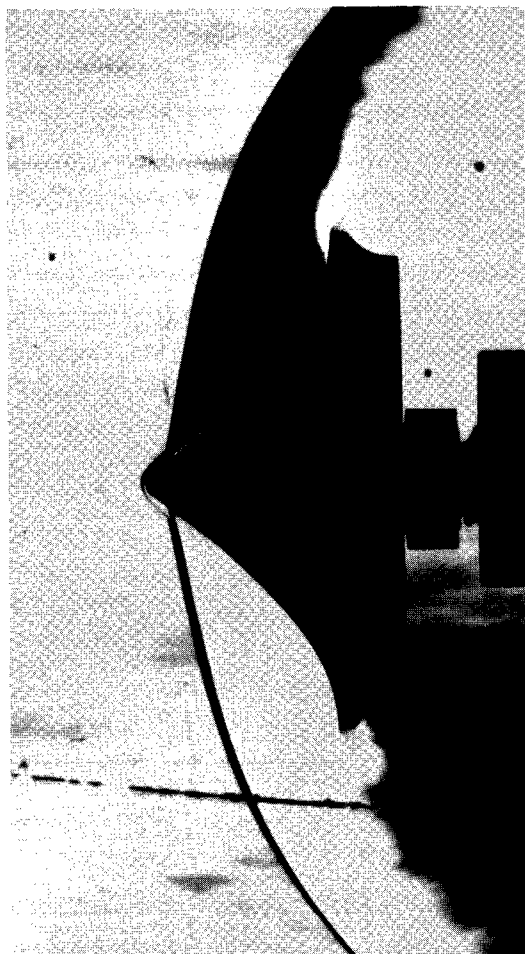
(d) $\beta_0 = 38.3^0$.
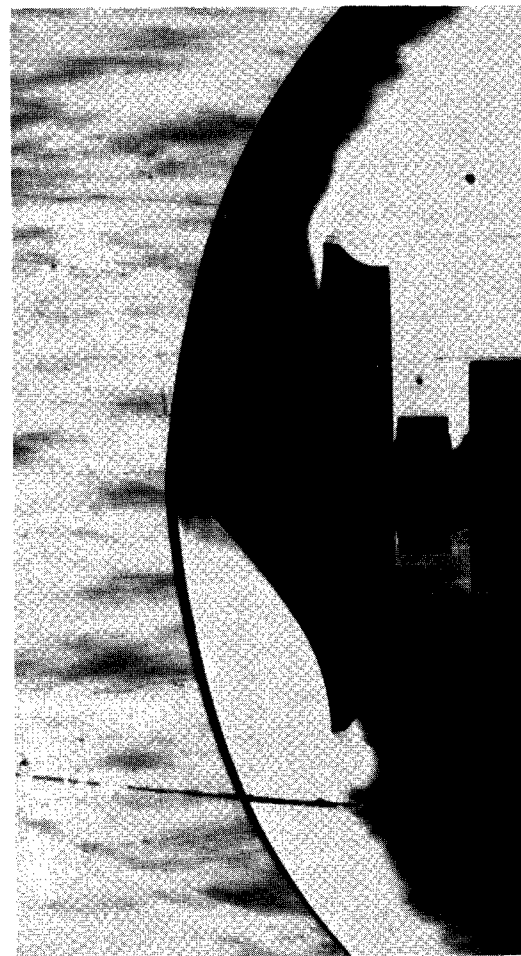
(e) $\beta_0 = 47.0^0$.

Figure 6.- Concluded.

L-66-4405

(a) $\beta_0 = 21.5^0$. (b) $\beta_0 = 27.0^0$. (c) $\beta_0 = 31.8^0$.
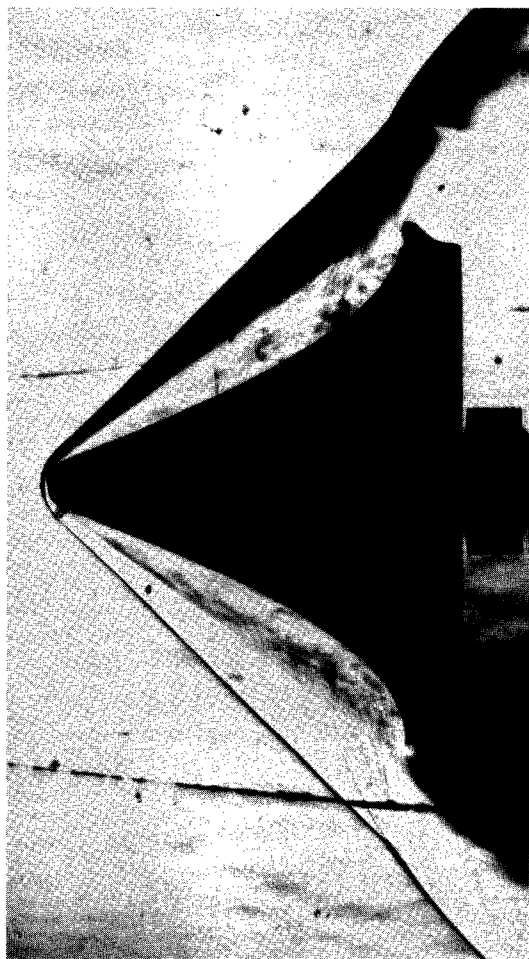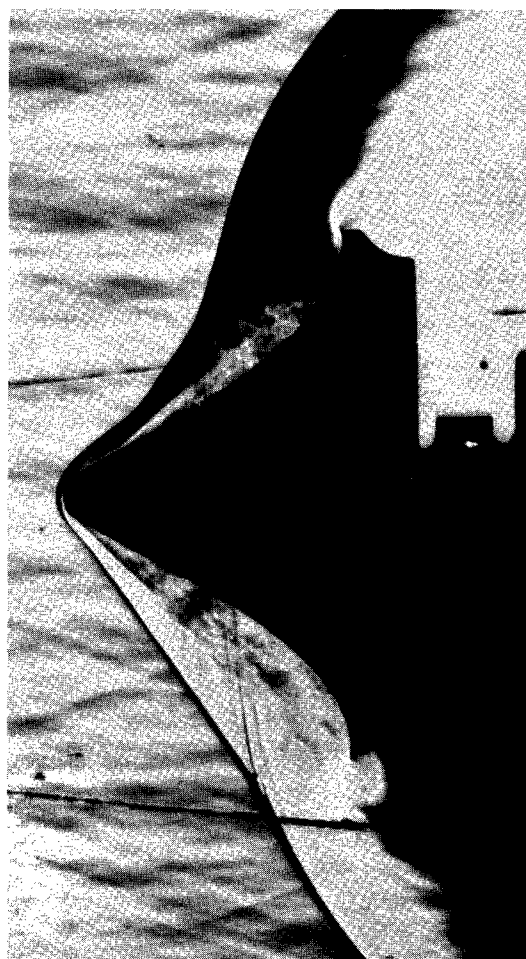
Figure 7.- Schlieren photographs of $\frac{N_\theta}{N_\varphi} = 0$ tension shell shapes. $\frac{r_n}{r_b} = 0.10$; $\alpha = 0^0$, $R \approx 3.0 \times 10^6$.

L-66-4406

(d) $\beta_0 = 38.3^0$.

(e) $\beta_0 = 47.0^0$.

Figure 7.- Concluded.

L-66-4407
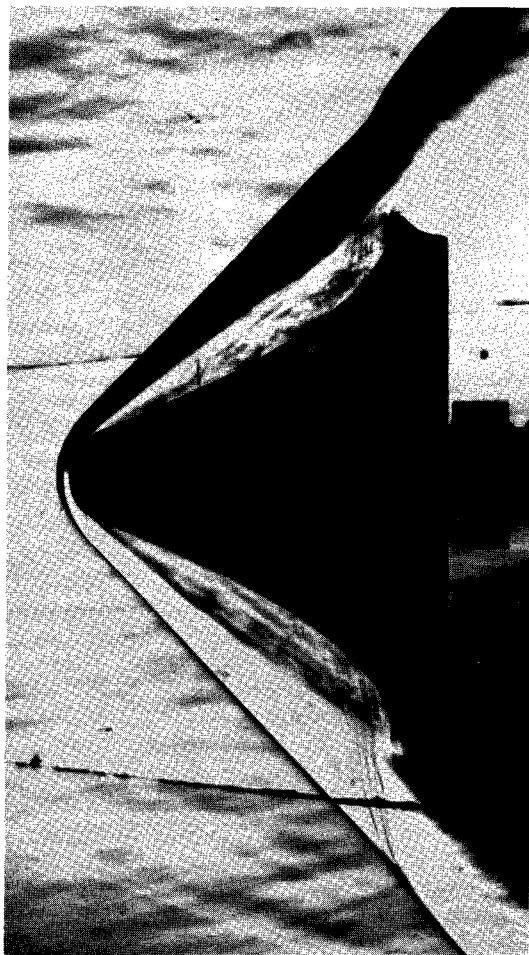
(a) $\beta_0 = 21.5^0$.
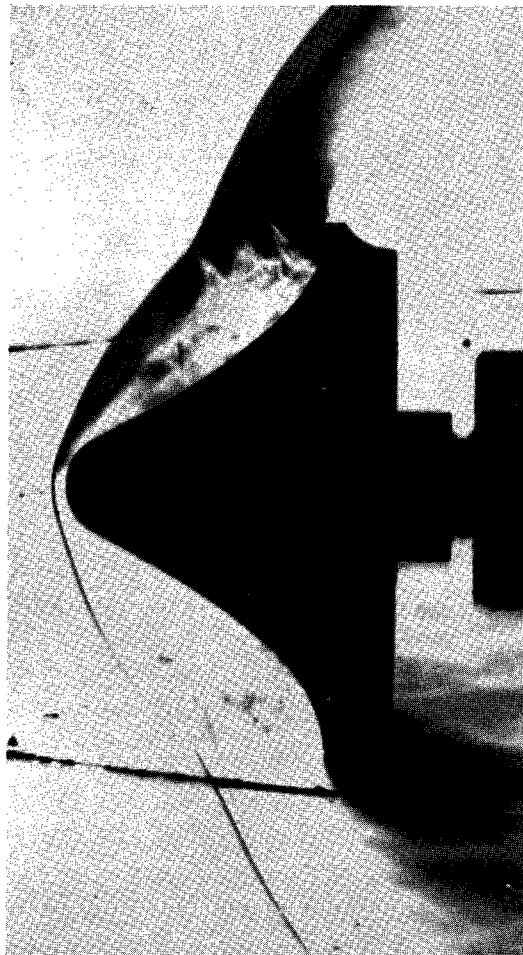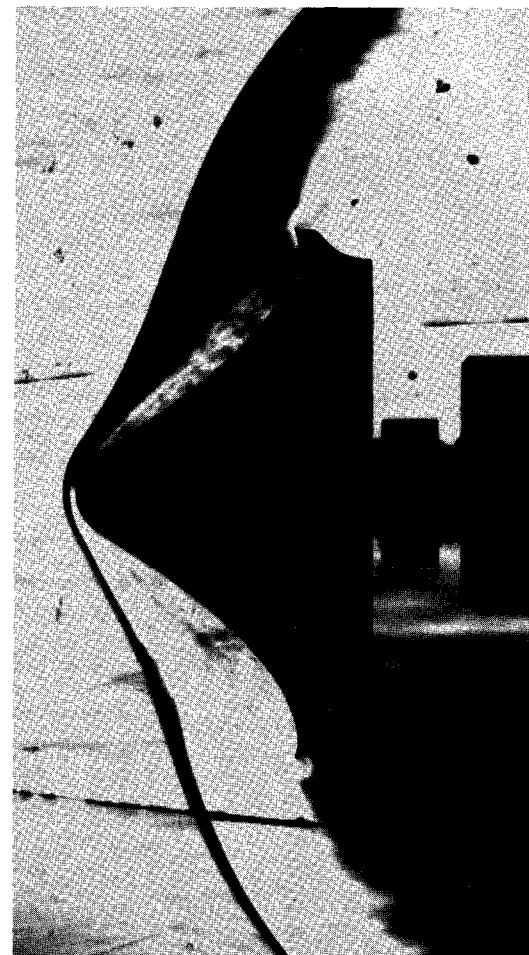
(b) $\beta_0 = 27.0^0$.

(c) $\beta_0 = 31.8^0$.

Figure 8.- Schlieren photographs of $\dfrac{N_\theta}{N_\varphi} = 0$ tension shell shapes. $\dfrac{r_n}{r_b} = 0.20$; $\alpha = 0^0$; $R \approx 3.0 \times 10^6$.

(d) $\beta_0 = 38.3^0$.

(e) $\beta_0 = 47.0^0$.

Figure 8.- Concluded.

L-66-4409
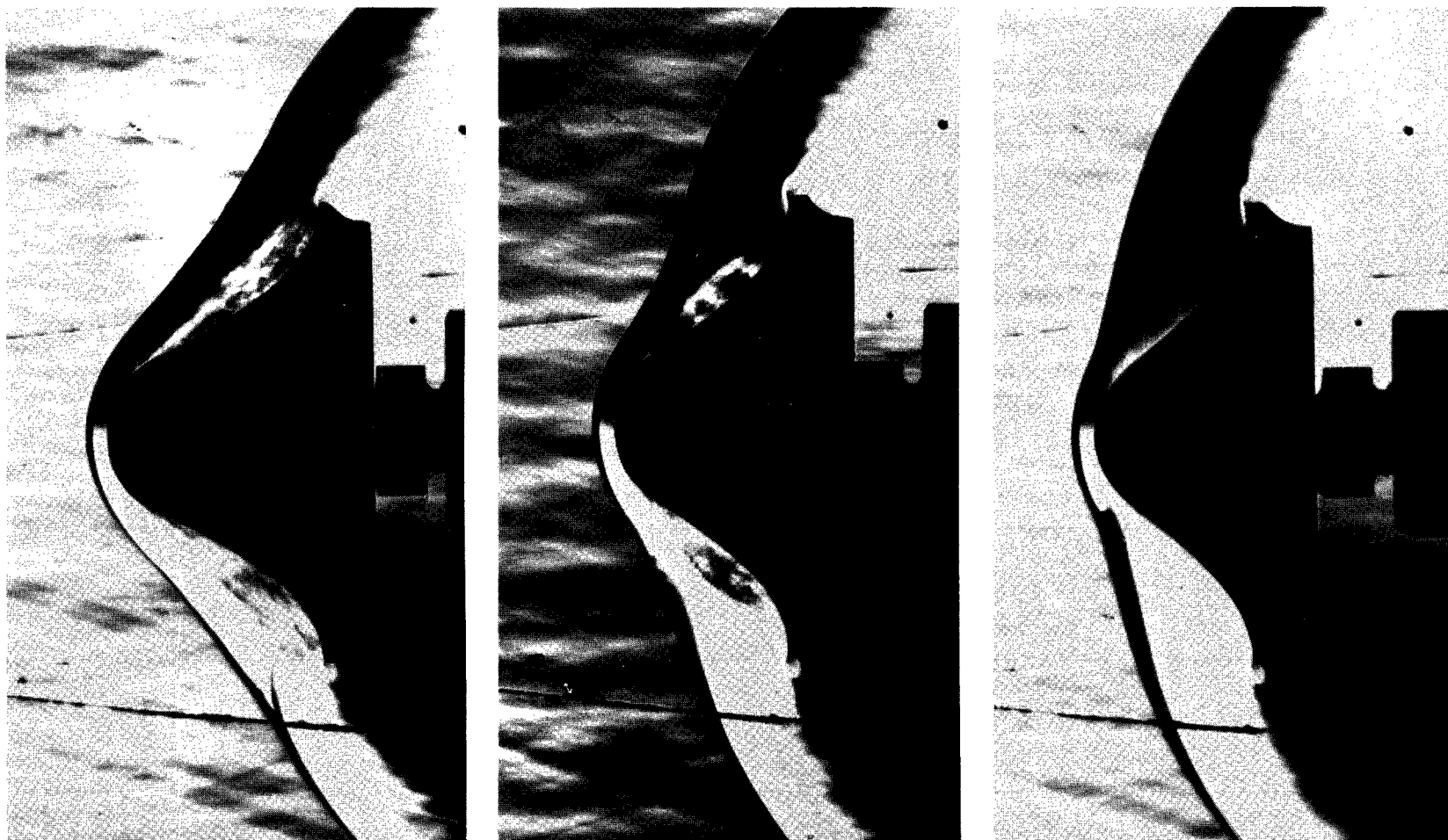
(a) $\beta_0 = 21.5^0$.

(b) $\beta_0 = 27.0^0$.

(c) $\beta_0 = 31.8^0$.

Figure 9.- Schlieren photographs of $\frac{N_\theta}{N_\varphi} = 0$ tension shell shape. $\frac{r_n}{r_b} = 0.40$; $\alpha = 0^0$; $R \approx 3.0 \times 10^6$.
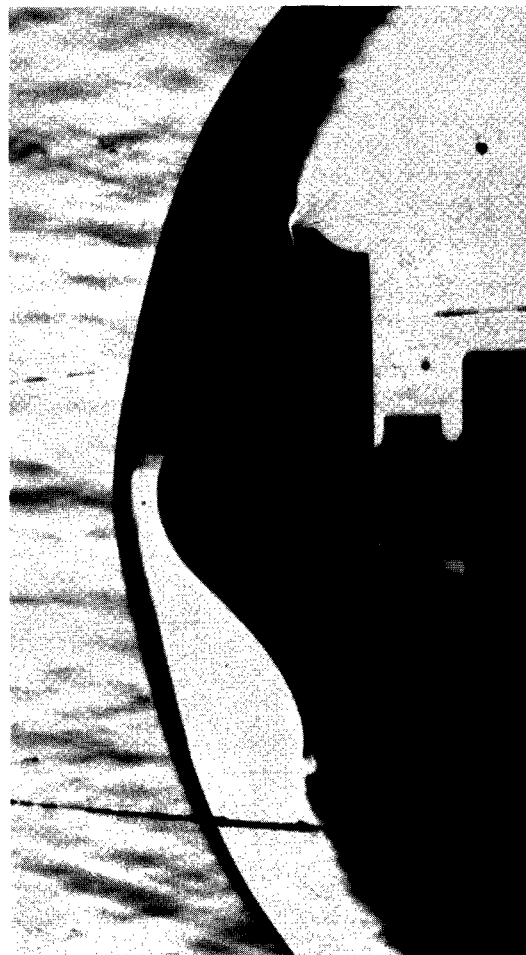
L-66-4410

(d) $\beta_0 = 38.3^0$.
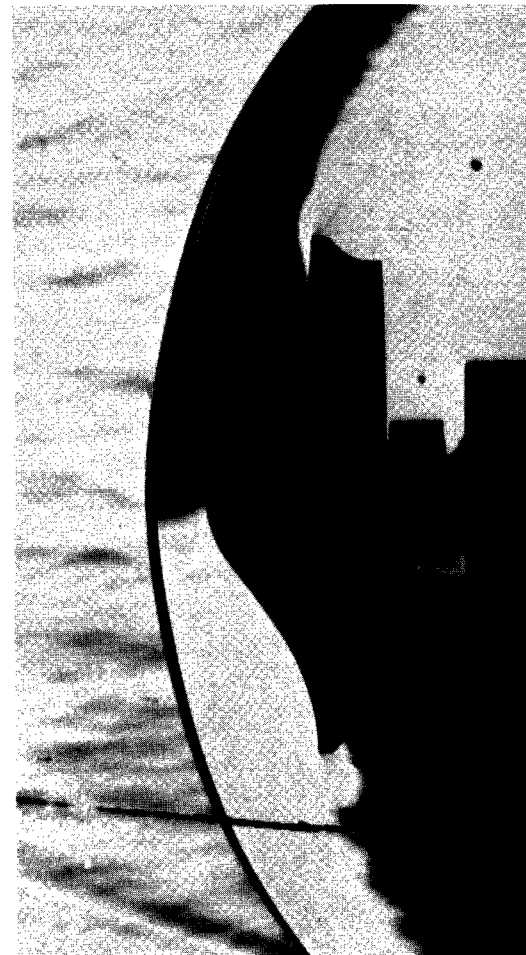
(e) $\beta_0 = 47.0^0$.

Figure 9.- Concluded.

L-66-4411

33
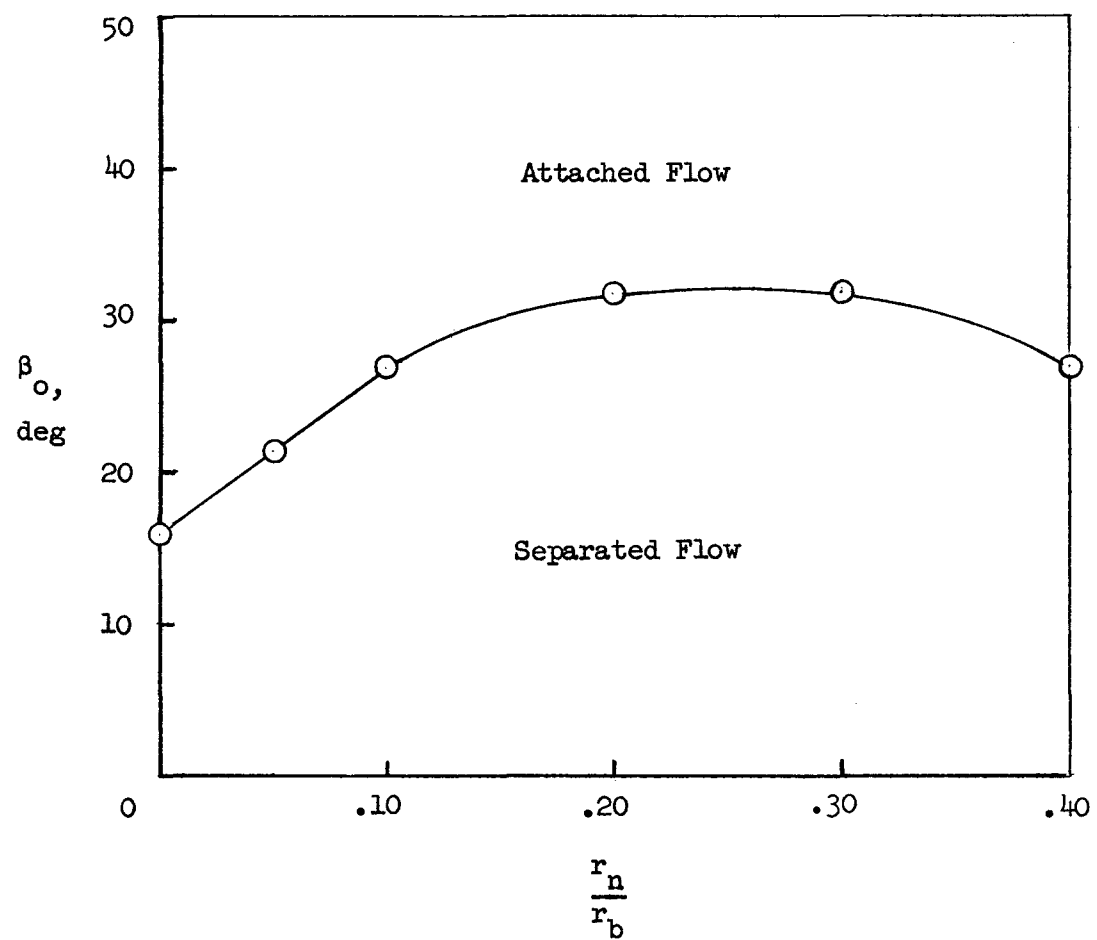
Figure 10.- Experimental variation of nose semivertex angle for flow separation with ratio of nose radius to base radius at $\alpha = 0^0$. $R \approx 3.0 \times 10^6$.
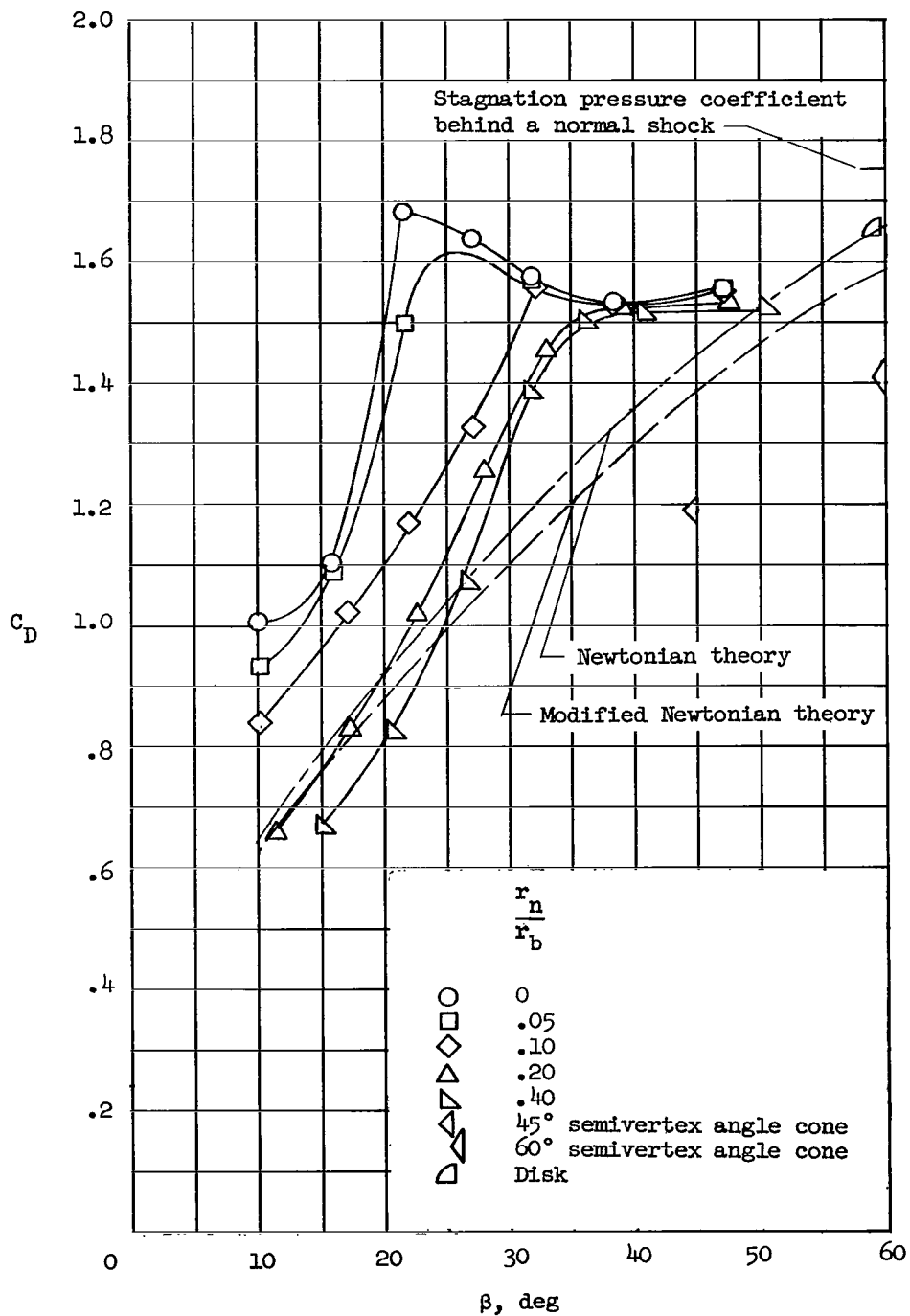
(a) M = 3.

Figure 11.- Effect of nose semivertex angle and spherical bluntness on drag coefficients at $\alpha = 0^{\circ}$. $R \approx 3.0 \times 10^6$.
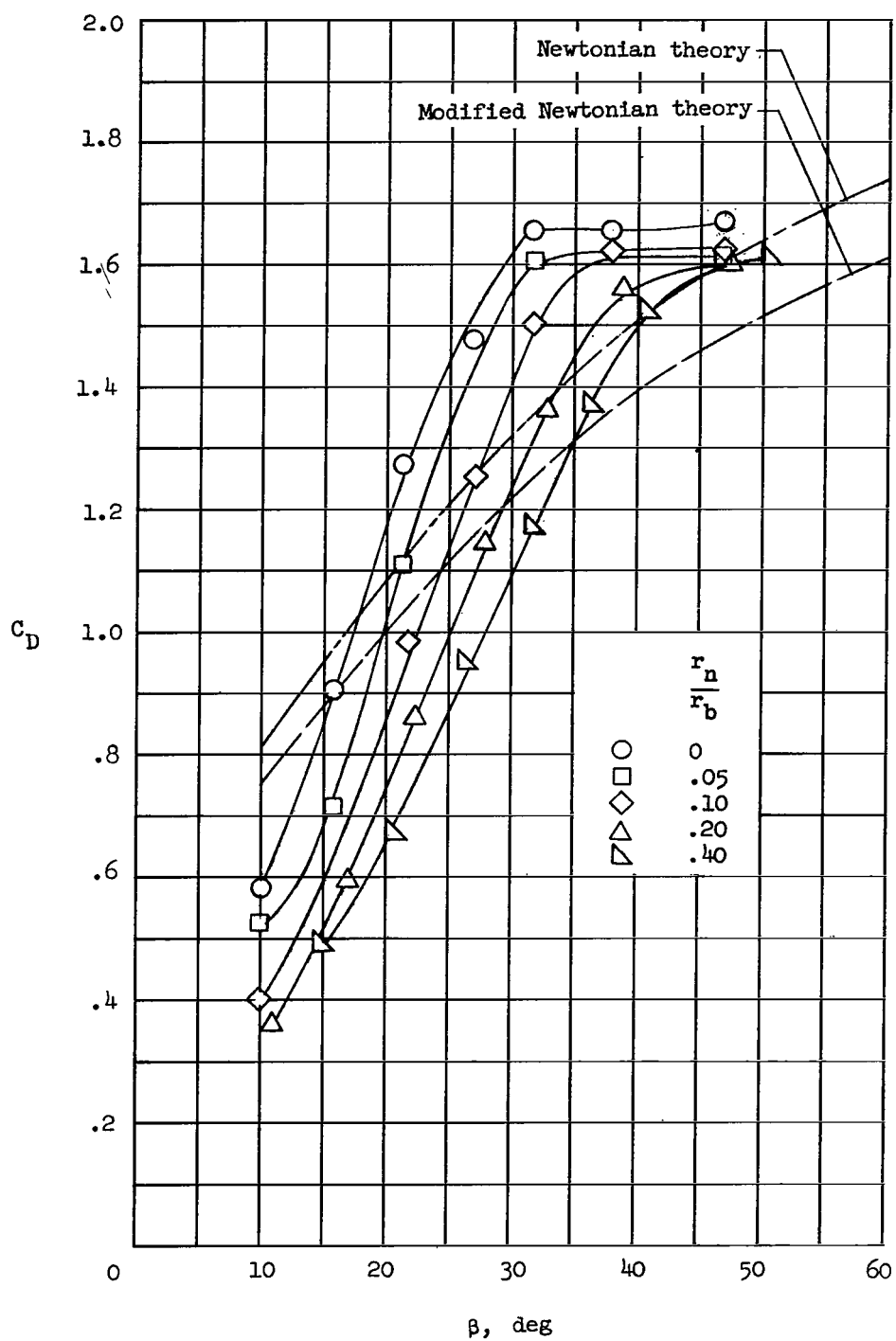
(b) M = 7.

Figure 11.- Concluded.
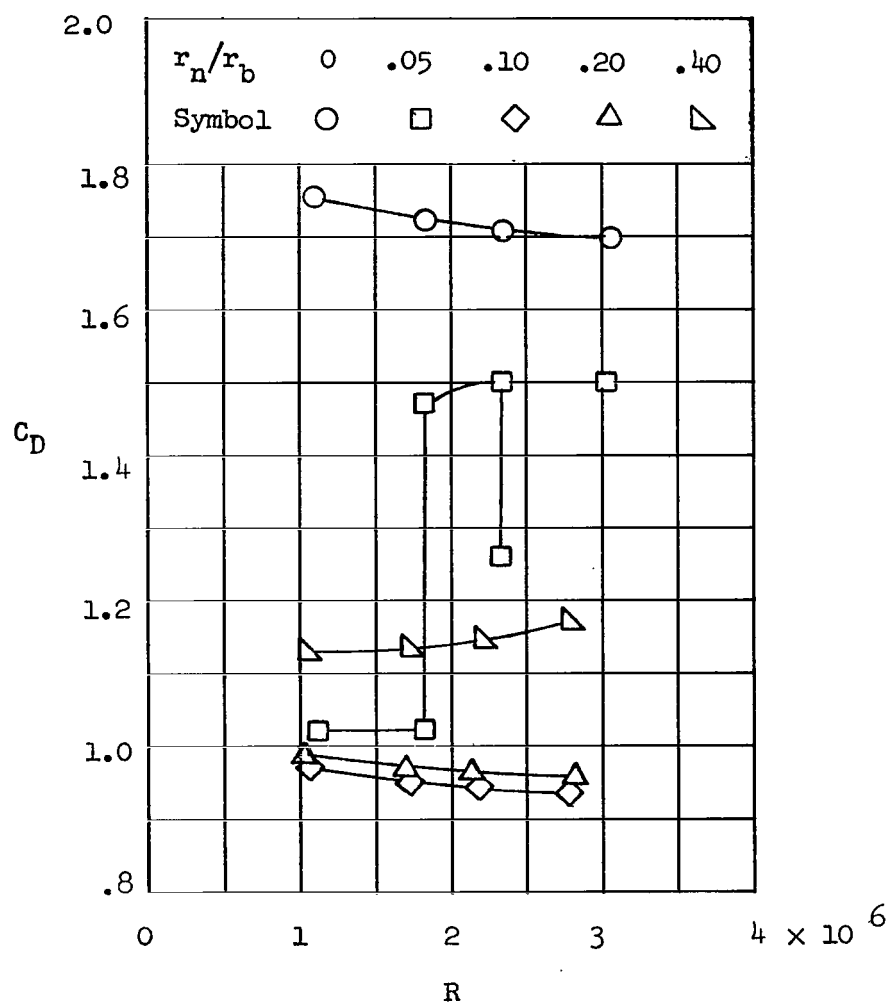
Figure 12.- Effect on drag coefficient due to Reynolds number for the $\frac{N_\theta}{N_\varphi} = 0$ tension shell shape for $\beta_0 = 21.5^0$. $\alpha = 0^0$.

Figure 13.- Schlieren photograph of $\frac{N_\theta}{N_\varphi} = 0$ tension shell shape for $\beta_0 = 27.0^0$ and $\frac{r_n}{r_b} = 0.05$ at an angle of attack of 3^0. $R \approx 3.0 \times 10^6$.
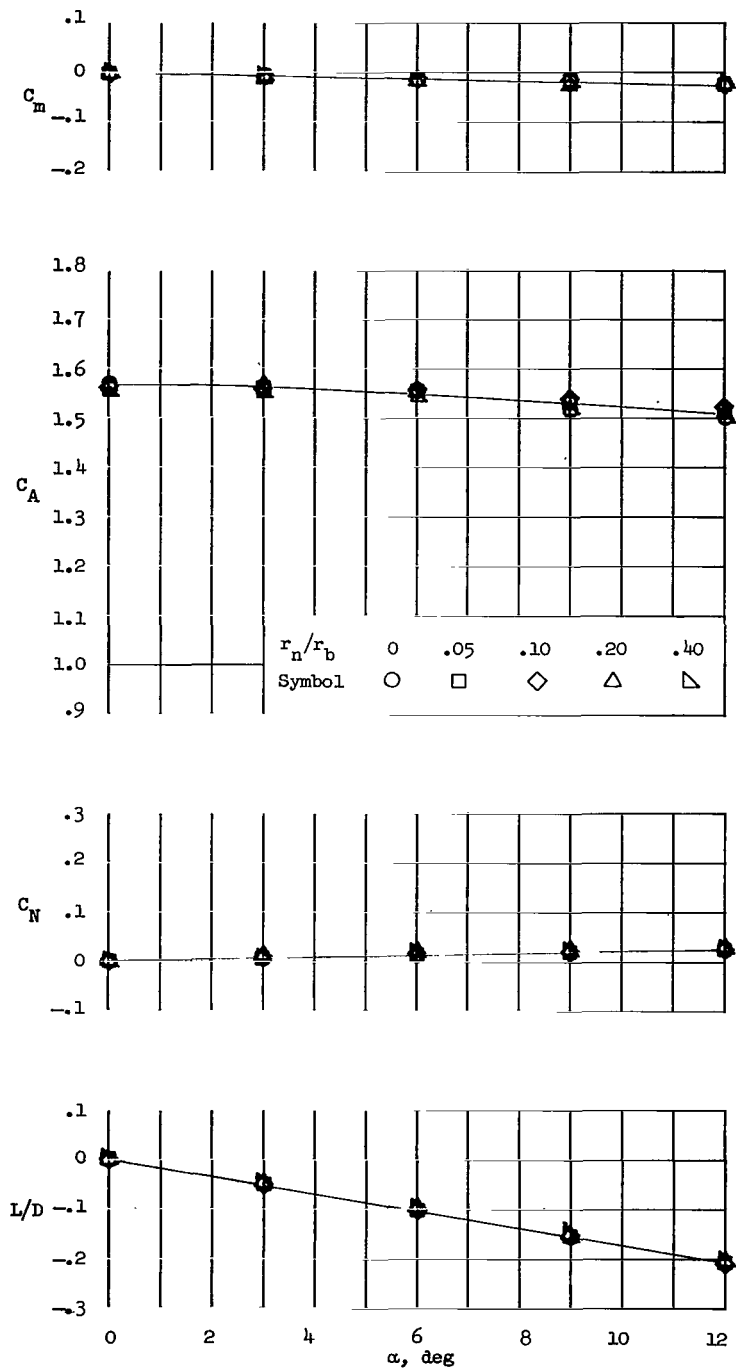
(a) $\beta_0 = 47.0^\circ$.

Figure 14.- Longitudinal aerodynamic characteristics of $\frac{N_\theta}{N_\varphi} = 0$ tension shell shapes. $R \approx 3.0 \times 10^6$.
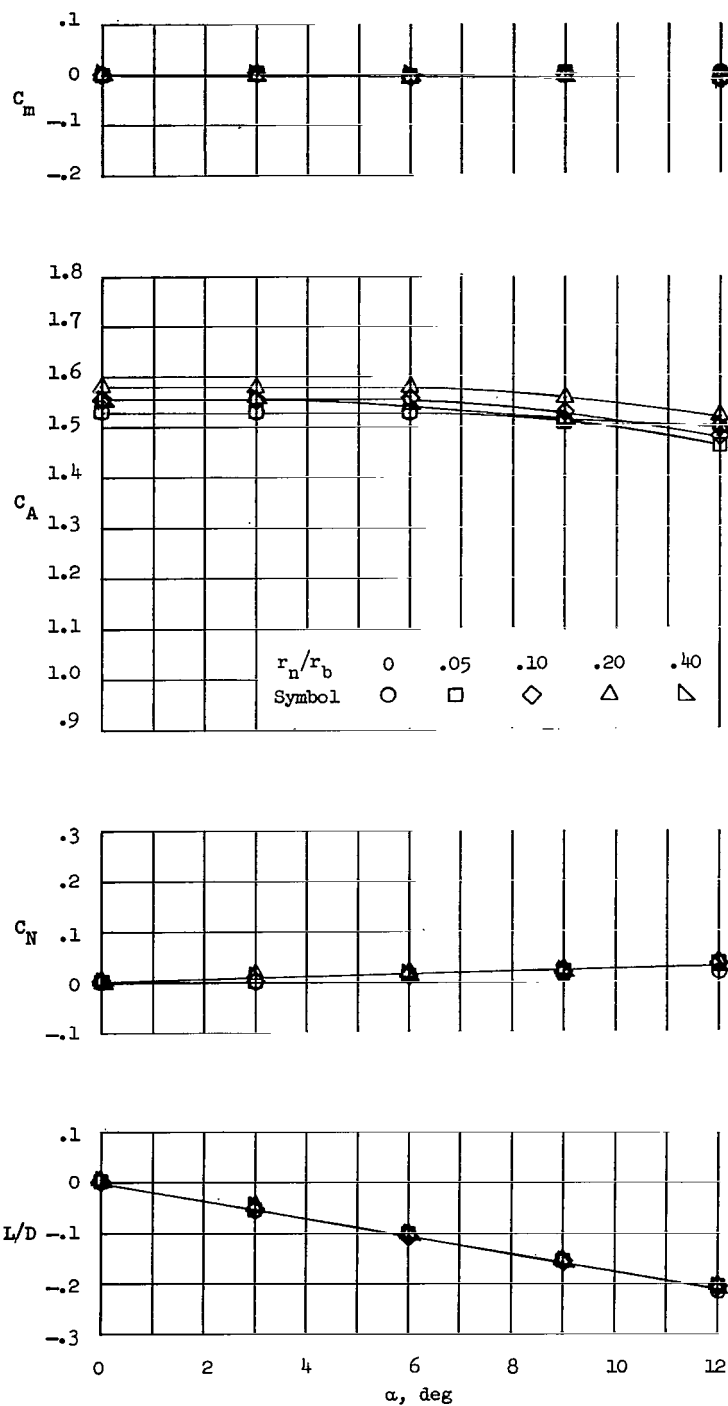
(b) $\beta_0 = 38.3^0$.

Figure 14.- Continued.
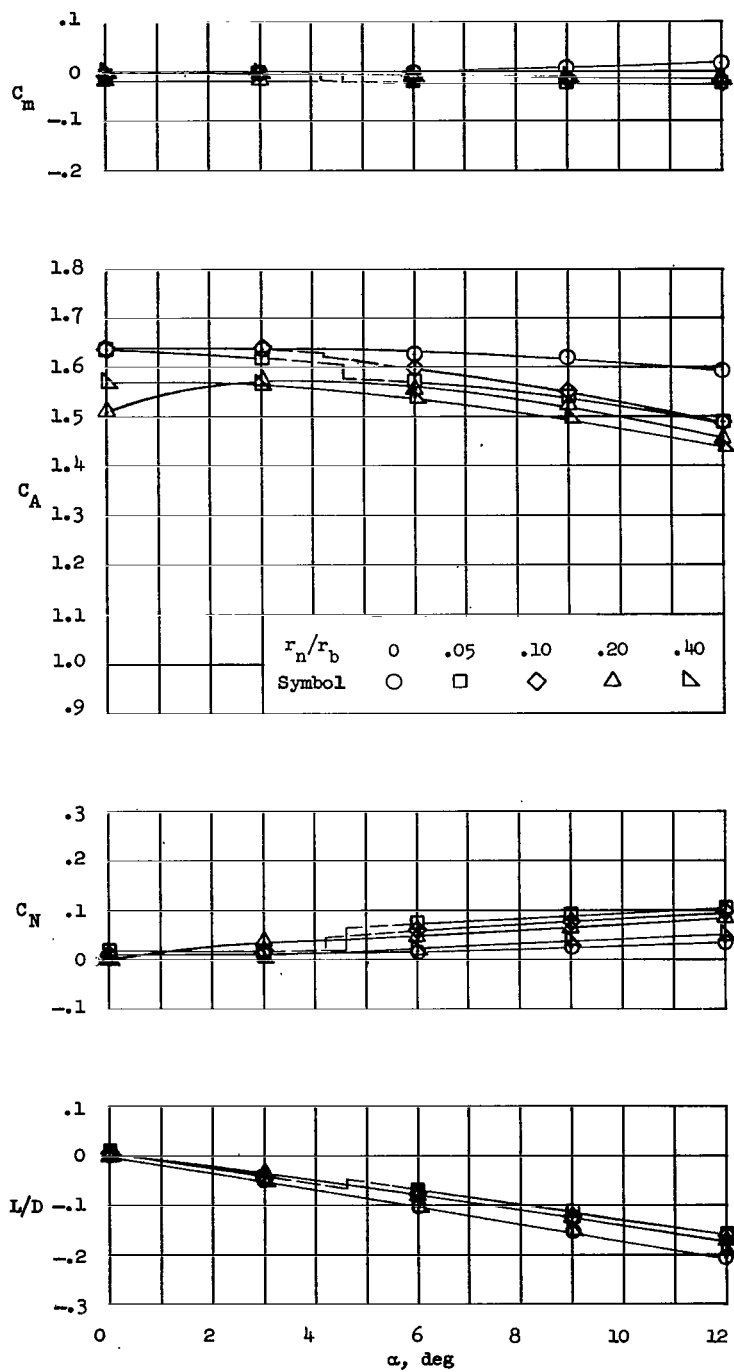
(c) $\beta_0 = 31.8^0$.

Figure 14.- Continued.
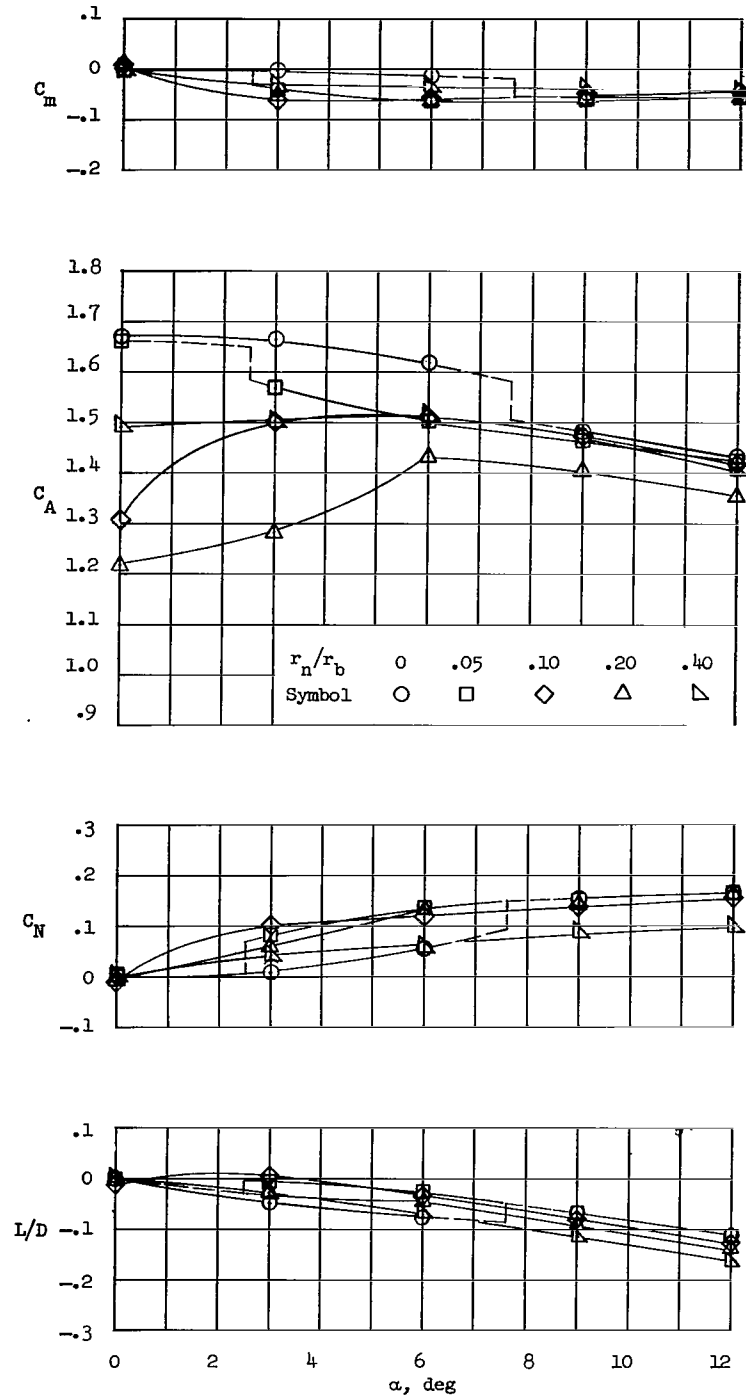
(d) $\beta_0 = 27.0^\circ$.

Figure 14.- Continued.
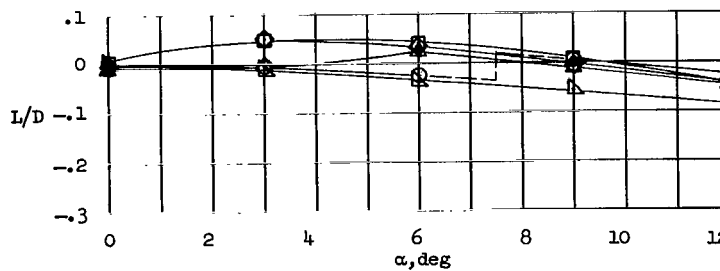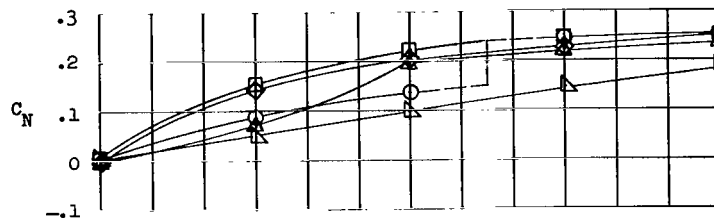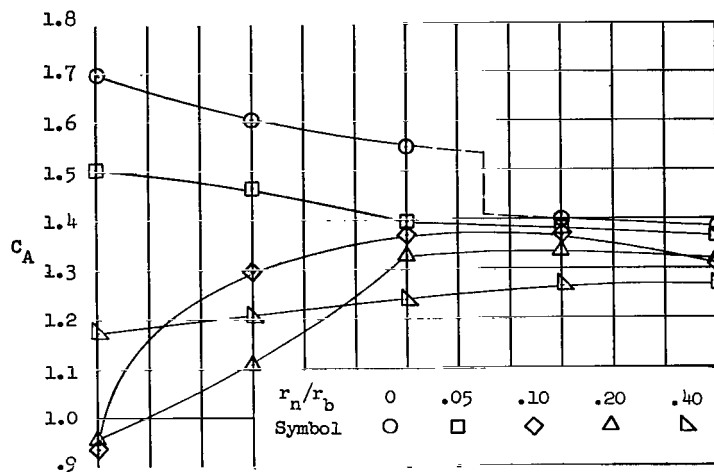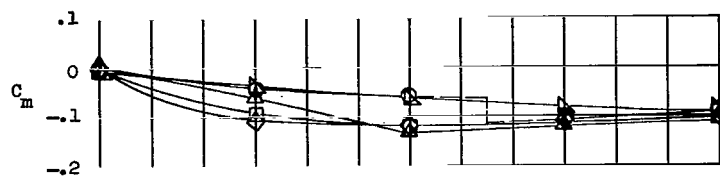
(e) $\beta_0 = 21.5^0$.

Figure 14.- Continued.
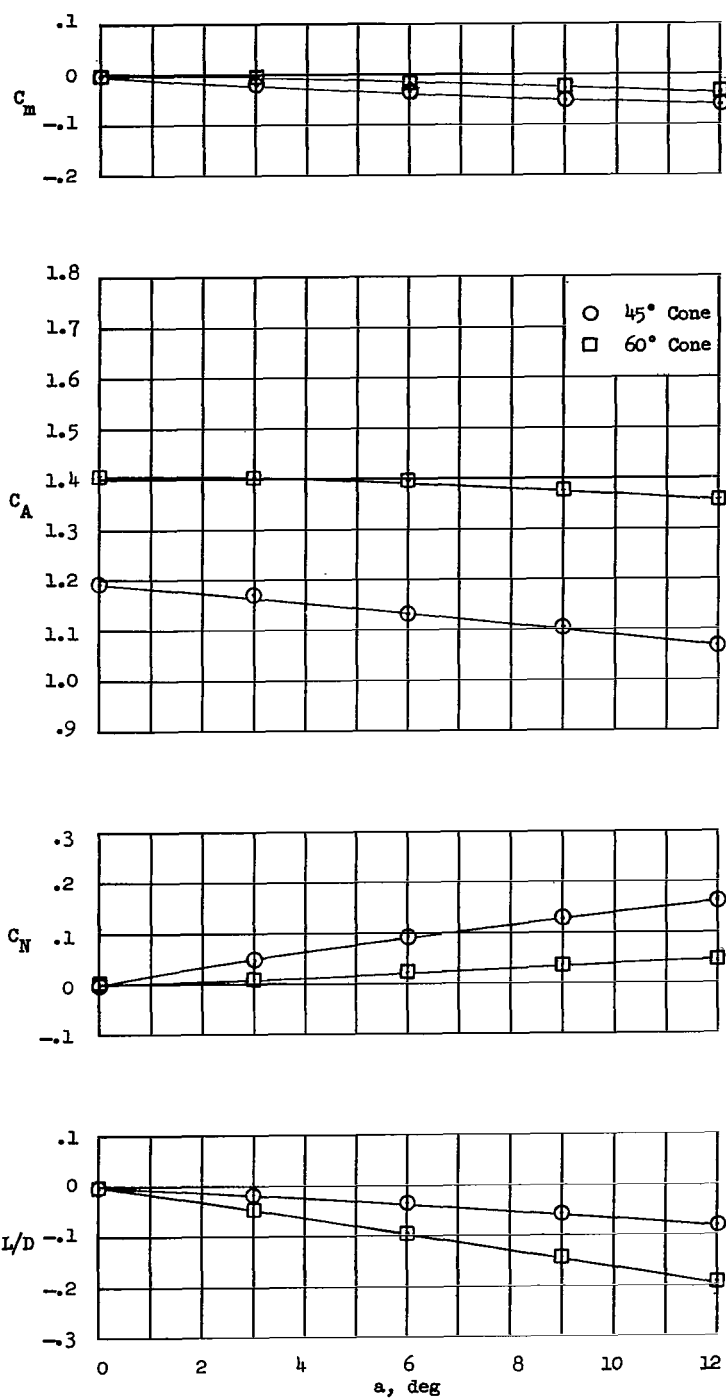
(f) Cone reference models.

Figure 14.- Concluded.

(a) $\dfrac{N_\theta}{N_\varphi} = 0.$
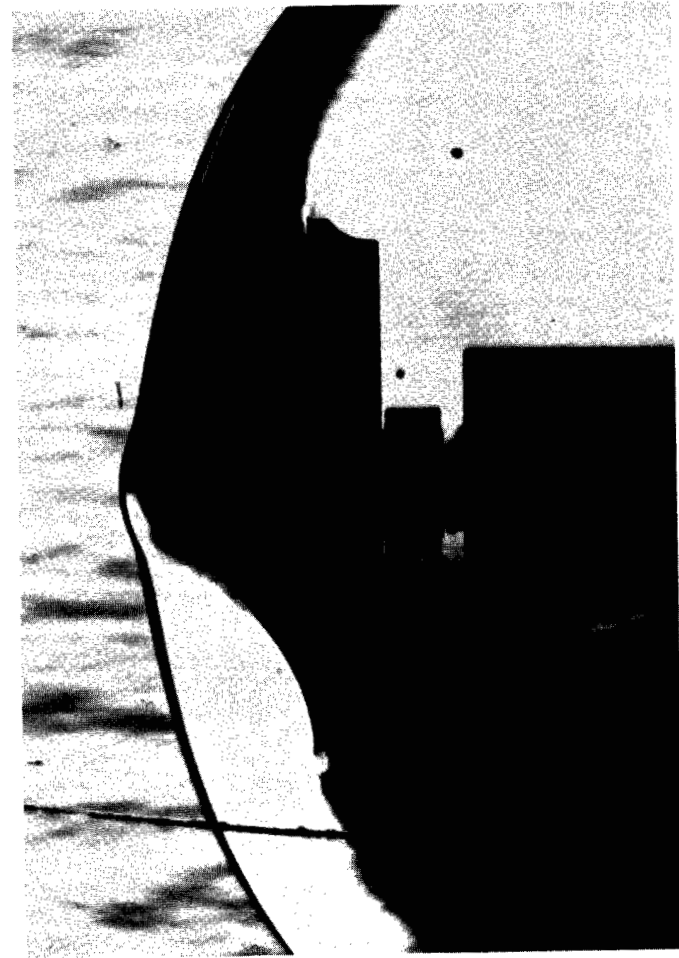
(b) $\dfrac{N_\theta}{N_\varphi} = 0.15.$

Figure 15.- Comparison of flow fields about tension shell shapes for $\dfrac{N_\theta}{N_\varphi} = 0$ and $\dfrac{N_\theta}{N_\varphi} = 0.15.$ $\dfrac{l}{r_b} = 0.555;$ $\alpha = 0^0;$ $R \approx 3.0 \times 10^6.$

L-66-4413

45

(a) $\dfrac{N_\theta}{N_\varphi} = 0$.   (b) $\dfrac{N_\theta}{N_\varphi} = 0.15$.   (c) $\dfrac{N_\theta}{N_\varphi} = 0.15$.

Figure 16.- Comparison of flow fields about tension shell shapes for $\dfrac{N_\theta}{N_\varphi} = 0$ and $\dfrac{N_\theta}{N_\varphi} = 0.15$. $\dfrac{l}{r_b} = 0.696$; $\alpha = 0^0$; $R \approx 3.0 \times 10^6$.

L-66-4414
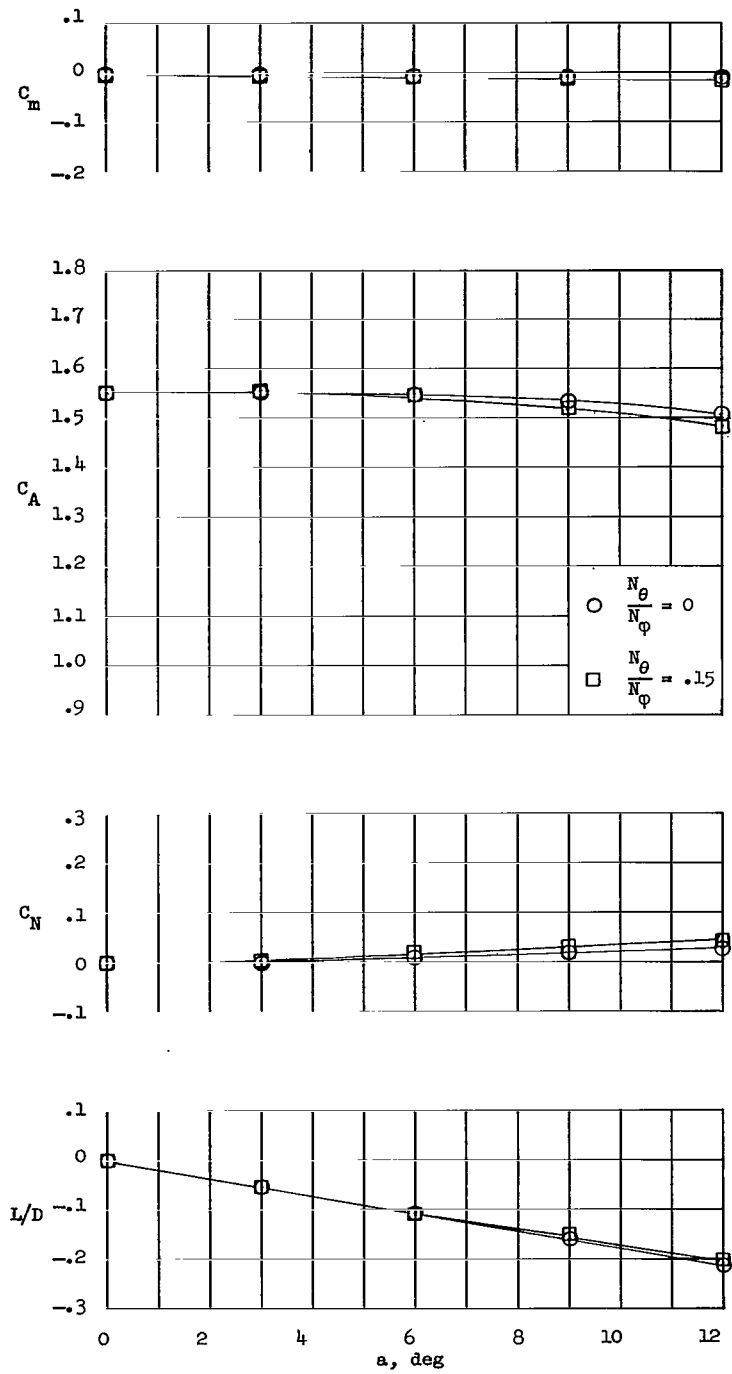
(a) $\frac{l}{r_b} = 0.555$.

Figure 17.- Comparison of longitudinal aerodynamic characteristics of $\frac{N_\theta}{N_\varphi} = 0$ and $\frac{N_\theta}{N_\varphi} = 0.15$ tension shell shapes. $R \approx 3.0 \times 10^6$.
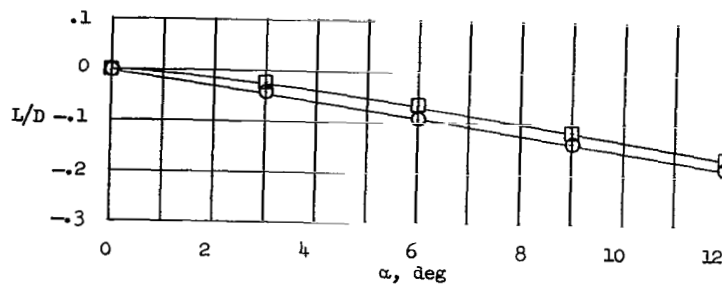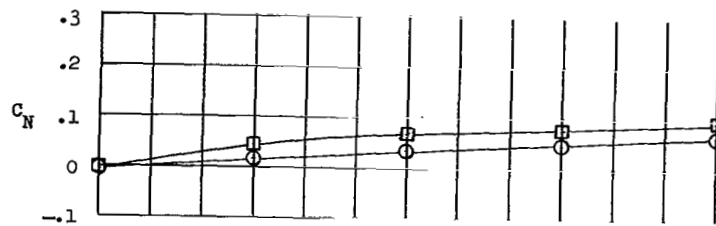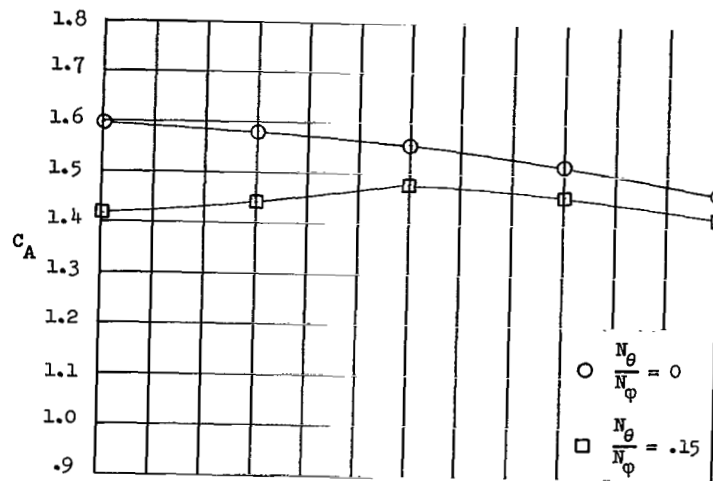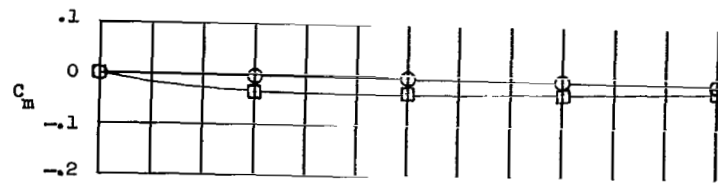
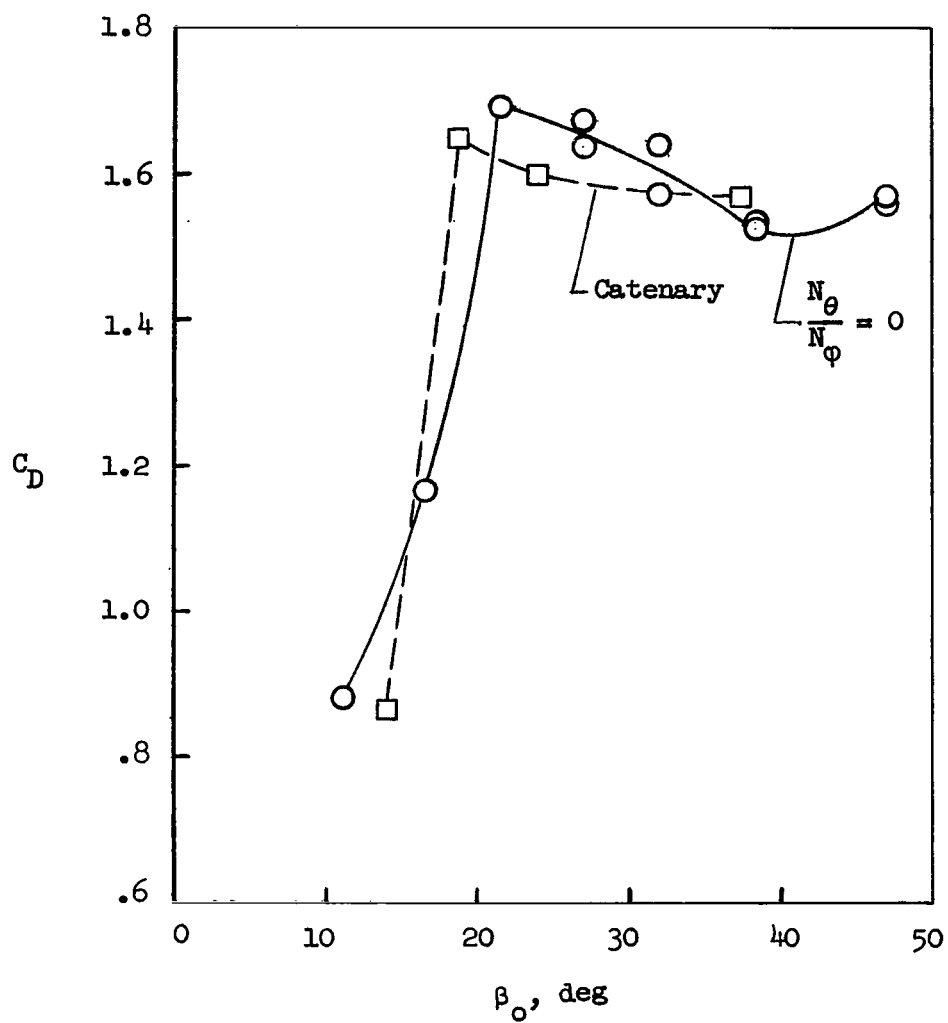(b) $\frac{l}{r_b} = 0.696$.

Figure 17.- Concluded.

Figure 18.- Comparison of drag coefficients of catenary shapes and $\dfrac{N_\theta}{N_\varphi} = 0$ tension shell shapes.

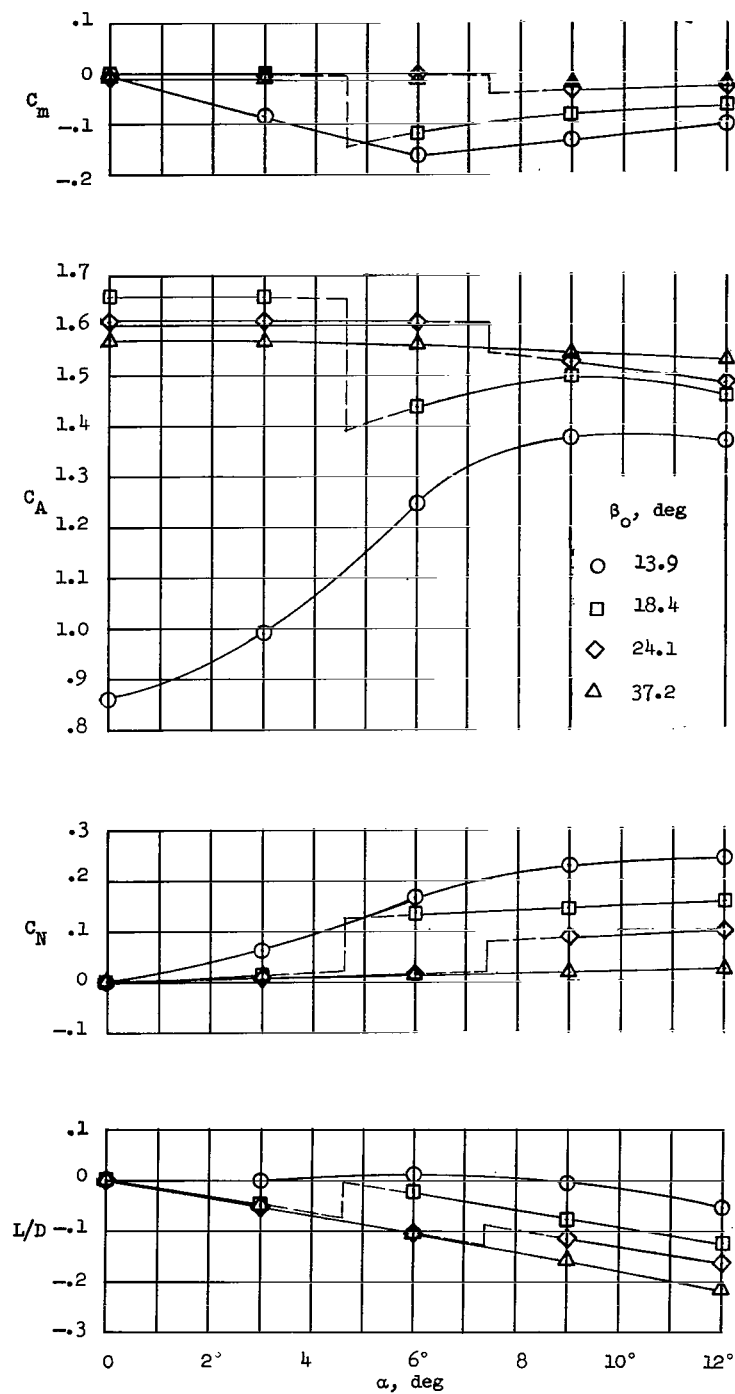$\alpha = 0^o$; $R \approx 3.0 \times 10^6$; $\dfrac{r_n}{r_b} = 0.$

Figure 19.- Longitudinal aerodynamic characteristics of catenary shapes. $R \approx 3.0 \times 10^6$.

"The aeronautical and space activities of the United States shall be conducted so as to contribute . . . to the expansion of human knowledge of phenomena in the atmosphere and space. The Administration shall provide for the widest practicable and appropriate dissemination of information concerning its activities and the results thereof."

—NATIONAL AERONAUTICS AND SPACE ACT OF 1958

NASA SCIENTIFIC AND TECHNICAL PUBLICATIONS

TECHNICAL REPORTS: Scientific and technical information considered important, complete, and a lasting contribution to existing knowledge.

TECHNICAL NOTES: Information less broad in scope but nevertheless of importance as a contribution to existing knowledge.

TECHNICAL MEMORANDUMS: Information receiving limited distribution because of preliminary data, security classification, or other reasons.

CONTRACTOR REPORTS: Technical information generated in connection with a NASA contract or grant and released under NASA auspices.

TECHNICAL TRANSLATIONS: Information published in a foreign language considered to merit NASA distribution in English.

TECHNICAL REPRINTS: Information derived from NASA activities and initially published in the form of journal articles.

SPECIAL PUBLICATIONS: Information derived from or of value to NASA activities but not necessarily reporting the results of individual NASA-programmed scientific efforts. Publications include conference proceedings, monographs, data compilations, handbooks, sourcebooks, and special bibliographies.

Details on the availability of these publications may be obtained from:

SCIENTIFIC AND TECHNICAL INFORMATION DIVISION

NATIONAL AERONAUTICS AND SPACE ADMINISTRATION

Washington, D.C. 20546